Journal of Zhejiang University-SCIENCE B 2025 26(12):1192-1215
www.jzus.zju.edu.cn; www.springer.com/journal/11585
E-mail: jzus_b@zju.edu.cn

Research Article
https://doi.org/10.1631/jzus.B2400132

Check for updates

Constructing a PANoptosis-based prognostic signature to evaluate the immune landscape and therapeutic response in clear cell renal cell carcinoma

Yu DONG[1*], Zitong YANG[2*], Zhinan XIA[3*], Jiahao LIAO[1], Zhiming CUI[4], Shenhao XU[1], Bing LIU[1], Liangliang REN[1], Tengda WANG[5], Wei GUO[1], Shuwen WANG[1], Yuyong WANG[6,7]✉, Cheng ZHANG[1]✉

[1]*Department of Urology, The Fourth Affiliated Hospital of School of Medicine, and International School of Medicine, International Institutes of Medicine, Zhejiang University, Yiwu 322000, China*
[2]*Department of Urology, Zhejiang Cancer Hospital, Hangzhou Institute of Medicine (HIM), Chinese Academy of Sciences, Hangzhou 310022, China*
[3]*Department of Urology, The Fourth Affiliated Hospital, Harbin Medical University, Harbin 150081, China*
[4]*Department of Radiology, The Fourth Affiliated Hospital of School of Medicine, and International School of Medicine, International Institutes of Medicine, Zhejiang University, Yiwu 322000, China*
[5]*Department of Urology, Guizhou Provincial People's Hospital, Guiyang 550002, China*
[6]*Department of Urology, Affiliated Hangzhou First People's Hospital, School of Medicine, Westlake University, Hangzhou 310006, China*
[7]*The Fourth School of Medicine Affiliated to Zhejiang Chinese Medical University, Hangzhou 310006, China*

Abstract: Objective: To identify pyroptosis, apoptosis, and necroptosis (PANoptosis)-related genes (PRGs) in clear cell renal cell carcinoma (ccRCC) for patient stratification and prognosis prediction. Methods: We used differential expression analysis and weighted gene co-expression network analysis (WGCNA) to identify ccRCC-specific PRGs. A prognostic model, the PANoptosis-index (PANI), was constructed using least absolute shrinkage and selection operator (LASSO) and Cox regression. The PANI model, comprising PRGs, was validated through single-cell RNA-sequencing (scRNA-seq), immunohistochemistry, and reverse transcription-quantitative polymerase chain reaction (RT-qPCR). Patient cohorts were categorized into high- and low-PANI groups, and the model's performance was appraised using various metrics. External validation was performed with the E-MTAB-1980 dataset. Functional and gene set enrichment analyses distinguished biological differences between groups. Mutational landscapes and tumor immune microenvironments were compared. Sensitivity to immunotherapy and antineoplastic drugs was also predicted using PANI. The effects of Z-DNA-binding protein 1 (*ZBP1*) on cell proliferation and migration were assessed by cell counting kit-8 (CCK-8) and Transwell assays. Results: We identified five PRGs (*ZBP1*, tumor necrosis factor superfamily protein 14 (*TNFSF14*), cyclin-dependent kinase inhibitor 3 (*CDKN3*), parathyroid hormone-like hormone (*PTHLH*), and heme-oxygenase 1 (*HMOX1*)) constituting PANI, independently associated with ccRCC patient prognosis. The PANI-based nomogram, integrated with clinical factors, demonstrated high predictive accuracy for prognosis. High-PANI patients exhibited distinct co-mutation patterns in ccRCC driver genes and lower survival probabilities, with an enriched immune-related functional profile, indicating an activated immune environment. These patients also showed increased sensitivity to immunotherapy and antineoplastic drugs. The knockdown of *ZBP1*, a key PRG in the PANI, significantly reduced ccRCC cell proliferation and migration. Conclusions: PANI provides precise prognosis and immunotherapy response predictions for ccRCC patients, facilitating individualized treatment strategies.

Key words: Pyroptosis, apoptosis, and necroptosis (PANoptosis); Clear cell renal cell carcinoma (ccRCC); Prognosis; Tumor immune microenvironment; Immunotherapy response

✉ Yuyong WANG, b1518118@zju.edu.cn
Cheng ZHANG, zhangcheng13836182568@zju.edu.cn
* The three authors contributed equally to this work
Yuyong WANG, https://orcid.org/0000-0002-7964-4436
Cheng ZHANG, https://orcid.org/0000-0003-3758-5172
Yu DONG, https://orcid.org/0000-0002-2744-2701
Zitong YANG, https://orcid.org/0000-0003-4716-1090
Zhinan XIA, https://orcid.org/0000-0003-0423-4405

Received Mar. 7, 2024; Revision accepted Nov. 29, 2024; Crosschecked Dec. 23, 2025

1 Introduction

Renal cell carcinoma ranks among the 16 most prevalent malignancies in the world. There are more than 430 000 newly diagnosed patients and 180 000 associated deaths annually (Sung et al., 2021). Clear cell renal cell carcinoma (ccRCC), the most frequently diagnosed pathological type, accounts for nearly 75%

of all cases. Most ccRCC patients are diagnosed at an early stage, making surgical treatment the primary approach (Santoni et al., 2024). However, 25%–30% of patients present with metastasis at diagnosis, and 30% experience recurrence after surgery, highlighting the need for systemic therapies (Allemani et al., 2018). One of the main strategies for managing advanced ccRCC is targeted therapy. Nevertheless, over time, a substantial number of patients develop resistance to the treatment (Capitanio and Montorsi, 2016). Immunotherapy is an effective option for late-stage ccRCC, as nearly 30% of patients exhibit programmed death-ligand 1 (PD-L1) overexpression (Rodriguez-Vida et al., 2017). However, not all patients achieve favorable outcomes with immunotherapy (Rini et al., 2019), and some may experience adverse events that limit its effectiveness (Dall'Olio et al., 2021; Guven et al., 2022; Rizzo et al., 2023). Hence, there is a critical need to establish accurate predictive models for ccRCC prognosis and immunotherapy response.

As research on crosstalk among cell death processes in various diseases has progressed (Lamkanfi et al., 2008; Malireddi et al., 2010; Gurung et al., 2014; Lukens et al., 2014; Kuriakose et al., 2016), the concept of "PANoptosis" (pyroptosis, apoptosis, and necroptosis) has emerged (Kuriakose et al., 2016; Malireddi et al., 2018, 2020; Zheng et al., 2020; Jiang et al., 2021; Karki et al., 2021b). PANoptosis represents an inflammatory form of programmed cell death (PCD) that integrates features of necroptosis, apoptosis, pyroptosis, and/or ferroptosis (Lin et al., 2022). Its initiation involves the regulatory interactions of Z-DNA-binding protein 1 (ZBP1), absent in melanoma 2 (AIM2), and pyrin, culminating in the formation of the AIM2-mediated PANoptosome, which includes diverse inflammasome sensors and crucial cell death regulators, including caspase-3, -7, and -8 in apoptosis, gasdermin-D (GSDMD), gasdermin-E (GSDME), and caspase-1 in pyroptosis, as well as mixed lineage kinase domain-like protein (MLKL) and receptor-interacting serine/threonine protein kinase 3 (RIPK3) in necroptosis (Lee et al., 2021).

Recent studies have elucidated the role of PANoptosis-related biomarkers in promoting anti-tumor immune responses (Karki et al., 2020, 2021a; Park et al., 2021). For instance, RIPK3 activation in colon cancer cells increases cytokine production within the tumor microenvironment (TME), enhancing cytotoxic antitumor immunity (Park et al., 2021). PANoptosis, by triggering systemic inflammation through the release of pro-inflammatory cellular contents, presents a promising strategy for solid tumor immunotherapy (Zhao et al., 2020).

Despite its potential, the role of PANoptosis in ccRCC is not well understood. Our study aimed to assess the prognostic importance of PANoptosis-related genes (PRGs) and to develop a prognostic model, the PANoptosis-index (PANI), for predicting ccRCC prognosis and immunotherapy responsiveness. We conducted a comprehensive evaluation and validation of this model using an external dataset, revealing the significant correlation between PANI and the tumor immune microenvironment. Hence, our findings could inform personalized treatment strategies and improve patient prognosis outcomes in ccRCC.

2 Materials and methods

2.1 Data collection and preprocessing

Transcriptional data (HTseq-counts form) of ccRCC and adjacent normal tissues were downloaded from The Cancer Genome Atlas Research Network (2013), with survival and clinical outcomes extracted from The Cancer Genome Atlas-Kidney Renal Clear Cell Carcinoma (TCGA-KIRC) bcrxml file. The transcriptional and clinical profiles of the E-MTAB-1980 project from the Array Express database were used as external validation datasets (Sato et al., 2013). The AnnoProbe package of the R environment was applied for probe identifier (ID) annotation. The baseline characteristics of the ccRCC patients are summarized in Tables 1 and 2. Single-cell RNA-sequencing (scRNA-seq) data of seven ccRCC patients were obtained from the publicly accessible dataset GSE156632 (Zhang et al., 2022). Additionally, we downloaded the IMvigor210 dataset, an external cohort of 348 patients treated with anti-programmed cell death protein 1 (anti-PD-1) therapy, to validate the immunotherapy response (Mariathasan et al., 2018). Immunohistochemical images for ccRCC were sourced from the Human Protein Atlas (HPA) database (Uhlén et al., 2015), while protein expression data were collected from the Clinical Proteomic Tumor Analysis Consortium (CPTAC) database (Ellis et al., 2013).

Table 1 Baseline characteristics of patients in The Cancer Genome Atlas-Kidney Renal Clear Cell Carcinoma (TCGA-KIRC)

Clinical feature	Subtype	Patient number	Patient percentage (%)
Age (years)	>65	185	34.5
	≤65	352	65.5
Gender	Male	346	64.4
	Female	191	35.6
Grade	G1	14	2.6
	G2	230	42.8
	G3	207	38.5
	G4	78	14.5
	Unknown	8	1.5
Stage	Stage I	269	50.1
	Stage II	57	10.6
	Stage III	125	23.3
	Stage IV	83	15.5
	Unknown	3	0.6
T-stage	T1	275	51.2
	T2	69	12.8
	T3	182	33.9
	T4	11	2.0
N-stage	N0	240	44.7
	N1	17	3.2
	Unknown	280	52.1
M-stage	M0	426	79.3
	M1	79	14.7
	Unknown	32	6.0

Table 2 Baseline characteristics of patients in E-MTAB-1980

Clinical feature	Subtype	Patient number	Patient percentage (%)
Age (years)	>65	95	39.6
	≤65	145	60.4
Gender	Male	184	76.7
	Female	56	23.3
Grade	G1	42	17.5
	G2	141	58.8
	G3	49	20.4
	G4	6	2.5
	Unknown	2	0.8
T-stage	T1	187	77.9
	T2	18	7.5
	T3	33	13.8
	T4	2	0.8
N-stage	N0	238	99.2
	N1	2	0.8
M-stage	M0	215	89.6
	M1	25	10.4

2.2 Identification of differentially expressed PRGs

A PRG list was generated in accordance with a previously published study (Sun et al., 2023) that extracted the gene list from the GeneCards database using a screening criterion of a relevance score greater than 3 (Stelzer et al., 2016). Differentially expressed genes (DEGs) between tumor and normal tissues were identified using the DESeq2 package in R (Love et al., 2014), with selection criteria of an absolute value of $\log_2$(fold change) of ⩾1 ($|(\log_2 FC)| \geqslant 1$) and a P value of <0.05.

2.3 Weighted gene co-expression network analysis (WGCNA)

A co-expression network for PRGs was generated using the R package "WGCNA" (Langfelder and Horvath, 2008). ccRCC samples were clustered through average linkage and Pearson correlation coefficients. The soft-threshold parameter for constructing the co-expression gene network was set at 7. To facilitate module identification, we calculated the topological overlap matrix (TOM) from the adjacency matrix, and then computed its dissimilarity measure. Genes exhibiting analogous expression profiles were grouped by constructing a hierarchical clustering tree, with network modules identified using a dynamic tree-cutting algorithm to segment the branches. The module with the highest correlation coefficient and strongest statistical significance was identified as the pivotal module, with its constituent genes selected for downstream analyses.

2.4 scRNA-seq data analysis

The scRNA-seq data analysis was conducted using the "Seurat" package (Stuart et al., 2019). Initially, quality control procedures were applied, retaining genes expressed in at least three cells, with mitochondrial gene content below 10%, and within an expression range of 200–7000. Next, 2000 highly variable genes were selected for further investigation. The "Harmony" package was used to address batch effects from different samples. Cell clusters were then identified using the "FindClusters" and "FindNeighbors" functions, with visualization performed via t-distributed stochastic neighbor embedding (t-SNE). Cells were annotated based on marker genes specific to different cell types. Finally, the "AddModuleScore" function

within Seurat was used to score each cell on its expression of the specific gene set of interest.

2.5 Model construction by machine learning approaches

Using the "createDataPartition" function in R, the ccRCC patients were randomly divided into training and testing cohorts at a 1:1 ratio. We initially identified potential prognostic PRGs via univariate Cox regression analysis, followed by least absolute shrinkage and selection operator (LASSO)-Cox regression using the "glmnet" package (Friedman et al., 2010) to further refine the selection of key prognostic PRGs. To optimize our model, we conducted a multivariate stepwise Cox regression to identify the most impactful PRGs and constructed a proportional hazards model. Based on this, we developed the PANI equation by integrating the multivariate regression coefficients (r) with the respective PRG expression levels (E_{PRG}): $PANI=\sum (E_{PRG}\times r)$.

Additionally, we performed Pearson correlation analysis to identify transcription factors (TFs) and enhancer RNAs (eRNAs) associated with the PRGs in our model, applying thresholds of an absolute value of Pearson correlation of >0.4 and $P<0.001$. The associations between identified TFs/eRNAs and PRGs were visualized using Sankey diagrams to illustrate potential regulatory relationships.

2.6 Survival analysis and nomogram construction

We categorized cohorts, including TCGA, internal training and testing datasets, and E-MTAB-1980, into high- and low-PANI groups using the median PANI value as the threshold. Kaplan-Meier (KM) survival analysis, conducted with the "survminer" R package, was used to assess differences in overall survival (OS) and progression-free survival (PFS) across these groups, with significance evaluated by the log-rank test ($P<0.05$). Using the "timeROC" package, receiver operating characteristic (ROC) curve analysis was used to measure the sensitivity and specificity of PANI for OS prediction in ccRCC patients, allowing us to compare PANI's area under the curve (AUC) with other clinical features.

To further refine our prognostic model and strengthen its predictive accuracy, we developed a nomogram that combines the PANI score with individual clinical characteristics, delivering a quantitative survival estimate for ccRCC patients. The precision, discriminative ability, and overall effectiveness of the nomogram were assessed using ROC analysis and the concordance index (C-index), ensuring robust prognostic utility.

2.7 Genomic alteration analysis

Each patient's variant file was retrieved from the TCGA repository. Using the "maftools" R package, we analyzed the mutated genes across different PANI categories and calculated the tumor mutation burden (TMB) for each individual (Mayakonda et al., 2018). This package was also used to generate an oncoplot that visualizes the landscape of genetic variants. Additionally, we used "maftools" to create a heatmap illustrating co-occurring variants, unrelated variants, and mutually exclusive variants, providing deeper insights into the genomic alterations associated with ccRCC in relation to the PANI score.

2.8 Functional enrichment analysis

We began our analysis by calculating the DEGs between the high- and low-PANI groups, ranking them according to their $\log_2$FC values. Following this, we used the "org.Hs.eg.db" and "clusterProfiler" R packages to perform functional enrichment analysis, including gene ontology (GO) analysis (Thomas et al., 2022) and gene set enrichment analysis (GSEA) on hallmark gene sets from the MSigDB database (Subramanian et al., 2005). GO enrichment analysis comprised the facets: biological process (BP), molecular function (MF), and cellular component (CC) (Thomas et al., 2022). The statistical significance threshold for GO enrichment analysis was set at $P<0.05$. We then visualized the top 10 most significantly enriched GO terms across the three categories (CC, BP, and MF), along with the top five most significant terms identified through GSEA.

2.9 Immune-related analysis

We used the "ESTIMATE" R package to evaluate the TME scores for the PANI groups, including the stromal score, immune score, and estimate score (Yoshihara et al., 2013). To quantify the immune microenvironment, we applied multiple algorithms, including "CIBERSORT," "EPIC," "MCP-counter," "quanTIseq," "TIMER," and "xCell" (Becht et al., 2016; Aran et al., 2017; Li et al., 2017; Chen et al.,

2018; Plattner et al., 2020). An immune modulator-related gene list was obtained from the GeneCards database and subsequently filtered by functional relevance score (Stelzer et al., 2016). We conducted a single-sample GSEA (ssGSEA) using the R package "gsva" (Hänzelmann et al., 2013) to assess the enrichment scores of immunocytes and the immune function-relevant pathways. Spearman correlation analysis was used to examine the relationships between the PANI score, immune cell fractions, and immune functions. Additionally, we performed correlation analysis to assess the relationship between PRG expression levels and immune functions.

2.10 Immunotherapy response prediction

The immunophenoscore (IPS), based on a machine learning algorithm developed from The Cancer Immunome Atlas (TCIA), was calculated for ccRCC patients based on their transcriptional data (van Allen et al., 2015). This score (including IPS, IPS-cytotoxic T lymphocyte-associated antigen-4 (CTLA4) blocker, IPS-PD-1/PD-L1/PD-L2 blocker, and IPS-CTLA4 and PD-1/PD-L1/PD-L2 blocker) (van Allen et al., 2015) serves as an indicator of their potential response to immunotherapy. IMvigor210, an external dataset comprising 348 patients who received anti-PD-1 treatment, was used to validate immune therapy responses.

2.11 Antineoplastic drug sensitivity prediction

The difference in half maximal inhibitory concentration (IC_{50}) between the groups was assessed by the Wilcoxon signed-rank test. The outcomes were then visually represented as box plots with the aid of "pRRophetic" and "ggplot2" (Geeleher et al., 2014).

2.12 Cell culture

The human ccRCC cell lines 786-O, A498, and OS-RC-2, as well as the human proximal renal tubular cell line HK-2 as a normal control, were procured from the American Type Culture Collection (ATCC; Manassas, VA, USA). All the cell lines were maintained in a culture medium supplemented with 10% (volume fraction) fetal bovine serum (FBS) and 1% (volume fraction) penicillin/streptomycin. The cells were incubated at 37 °C in a humidified atmosphere with 5% CO_2. Specifically, RPMI-1640 medium was used for OS-RC-2 and 786-O cells, whereas A498 and HK-2 cells were maintained in minimum essential medium (MEM) with the addition of non-essential amino acids.

2.13 RNA extraction and RT-qPCR

The total RNAs of 786-O, A498, OS-RC-2, and HK-2 cells were isolated using the FastPure Cell/Tissue Total RNA Isolation Kit V2 from Vazyme (Nanjing, China). Reverse transcription was subsequently conducted using the HiScript® III 1st Strand cDNA Synthesis Kit (+DNA-guided (gDNA) wiper) from Vazyme. Reverse transcription-quantitative polymerase chain reaction (RT-qPCR) was carried out using Taq Pro Universal SYBR qPCR Master Mix from Vazyme. Gene expression levels were assessed using the $2^{-\Delta\Delta C_T}$ method, with glyceraldehyde 3-phosphate dehydrogenase (*GAPDH*) serving as the endogenous control. These experiments were carried out three times. The primer sequences for *ZBP1*, cyclin-dependent kinase inhibitor 3 (*CDKN3*), tumor necrosis factor superfamily protein 14 (*TNFSF14*), parathyroid hormone-like hormone (*PTHLH*), and heme-oxygenase 1 (*HMOX1*) are provided in Table 3.

Table 3 Primer sequences for five PRGs

PRG	Primer sequence (5'→3')
ZBP1	F: AGAAGAGCAAAGTCAGCCTCAA R: CCAGCTGTTGGGTCCATTCT
CDKN3	F: ATCCAATCGCAGATGGAGGG R: GGAGACAAGCAGCTACAAGACA
TNFSF14	F: CTCTTGCTGTTGCTGATGGG R: TCGTGAGACCTTCGCTCTTGT
PTHLH	F: GTTCGAGGTTCAAAGGTTTGCC R: AGGTTGGAGGCGAGTTGAAAA
HMOX1	F: AGTTCAAGCAGCTCTACCGC R: ACTCCTCAAAGAGCTGGATGT

PRG: PANoptosis-related gene; F: forward; R: reverse.

2.14 Cell transfection

We purchased three small interfering RNAs (siRNAs) targeting *ZBP1* from GenePharma (China). The cells were transfected with 20 nmol/L of siRNA using jetPRiME (Polyplus, NY, USA) according to the manufacturer's protocol. The sequences used for the siRNAs are listed below: si-#1, sense 5'-CUUC GUUUGAAGCAAGAAUTT-3', antisense 5'-AUUCU UGCUUCAAACGAAGTT-3'; si-#2, sense 5'-CAA GUCCUCUACCGAAUGATT-3', antisense 5'-UCAUU

CGGUAGAGGACUUGT-3'; si-#3, sense 5'-GAUG AGCAGUCCAAAGCAUTT-3', antisense 5'-AUGC UUUGGACUGCUCAUCT-3'. The effectiveness of *ZBP1* knockdown was evaluated through RT-qPCR.

2.15 CCK-8 assay

Cell proliferation was assessed using the cell counting kit-8 (CCK-8; #C0038, Beyotime, Shanghai, China). The cells from both the experimental and control groups were plated in a 96-well plate at a density of 1000 cells per well. The proliferation of 786-O and OS-RC-2 cells was evaluated using the CCK-8 reagent (Beyotime) at 0, 24, 48, and 72 h post-seeding, with a final concentration of 10 μL per well. An automated microplate reader was used to determine the optical density of the reaction mixture at 450 nm.

2.16 Transwell assay

The Transwell migration assay was conducted using 24-well Transwell chambers (Corning, NY, USA). About 20 000 cells were suspended in serum-free medium and then placed into the upper chamber. In the lower chamber, culture medium containing 10% FBS was added as a chemoattractant. The cells that migrated across the membrane were fixed, stained, and counted under a light microscope (#CKX53, OLYMPUS, Tokyo, Japan), using ImageJ software for enumeration.

2.17 Wound healing assay

The cells were seeded in 6-well plates and grown to confluence overnight. A scratch was made in the monolayer using a sterile 200 μL pipette tip, and the wells were washed with phosphate-buffered saline (PBS) to remove detached cells. Fresh medium without FBS was added, and incubation was carried out for 24 h in a 5% CO_2 atmosphere at 37 ℃. Images of the wound area were captured at 0 and 24 h using a phase-contrast microscope (#BX43, OLYMPUS). Wound closure was quantified by measuring the area at each time point and calculating the percentage of closure using ImageJ.

2.18 Statistical analysis

Statistical analyses were conducted using R software (version 4.2.3) and GraphPad Prism (version 9.0.0). Correlation coefficients were assessed using Pearson analysis. Statistical significance was defined as a P value of <0.05.

3 Results

3.1 Identification of candidate PRGs in ccRCC and construction of PANI

A total of 935 PRGs were compiled (Table S1). Differential expression analysis on these PRGs using TCGA-KIRC transcriptional data identified 274 DEGs. Among them, 64 were downregulated in tumor samples and 210 were upregulated (Figs. 1a and 1b; Table S2). We then applied the WGCNA method to explore co-expression networks in the TCGA-KIRC dataset. A scale-free network was constructed with a soft-thresholding power of β=7 (Figs. S1a and S1b), followed by average linkage hierarchical clustering to identify three distinct gene modules (Figs. 1c and S1c–S1f). The MEblue module showed the strongest association with tumor samples (r=0.63, P<0.001; Fig. 1d), underscoring its clinical relevance. Within this module, 211 PRGs were confirmed to be tumor-related. By overlapping these PRGs with the DEGs, we identified 146 target genes significantly correlated with ccRCC (Fig. 1e).

The TCGA-KIRC patient cohort was randomly divided into a training set (n=267) and a testing set (n=266), maintaining an approximate 1:1 distribution. Using univariate Cox regression analysis, we initially identified 35 PRGs associated with OS in TCGA-KIRC patients (Fig. 1f). To refine these, we applied a LASSO-Cox proportional hazards regression, focusing on highly variable PRGs and integrating clinical data. This approach highlighted 12 PRGs as significant prognostic factors, which were then subjected to a multivariate stepwise Cox regression analysis for further refinement (Figs. 1g and 1h). The outcome was the development of a prognostic signature, termed PANI, for ccRCC, which is composed of five key PRGs (Fig. 1i).

We calculated Pearson correlation coefficients using multivariate Cox regression analysis and derived the PANI using the formula: $PANI=-0.001\,593\times E_{HMOX1}+0.031\,630\times E_{TNFSF14}+0.088\,565\times E_{CDKN3}+0.001\,691\times E_{PTHLH}+0.152\,944\times E_{ZBP1}$, where E is the expression level. Using the median PANI as the threshold, all patients were categorized into high- and low-PANI groups.

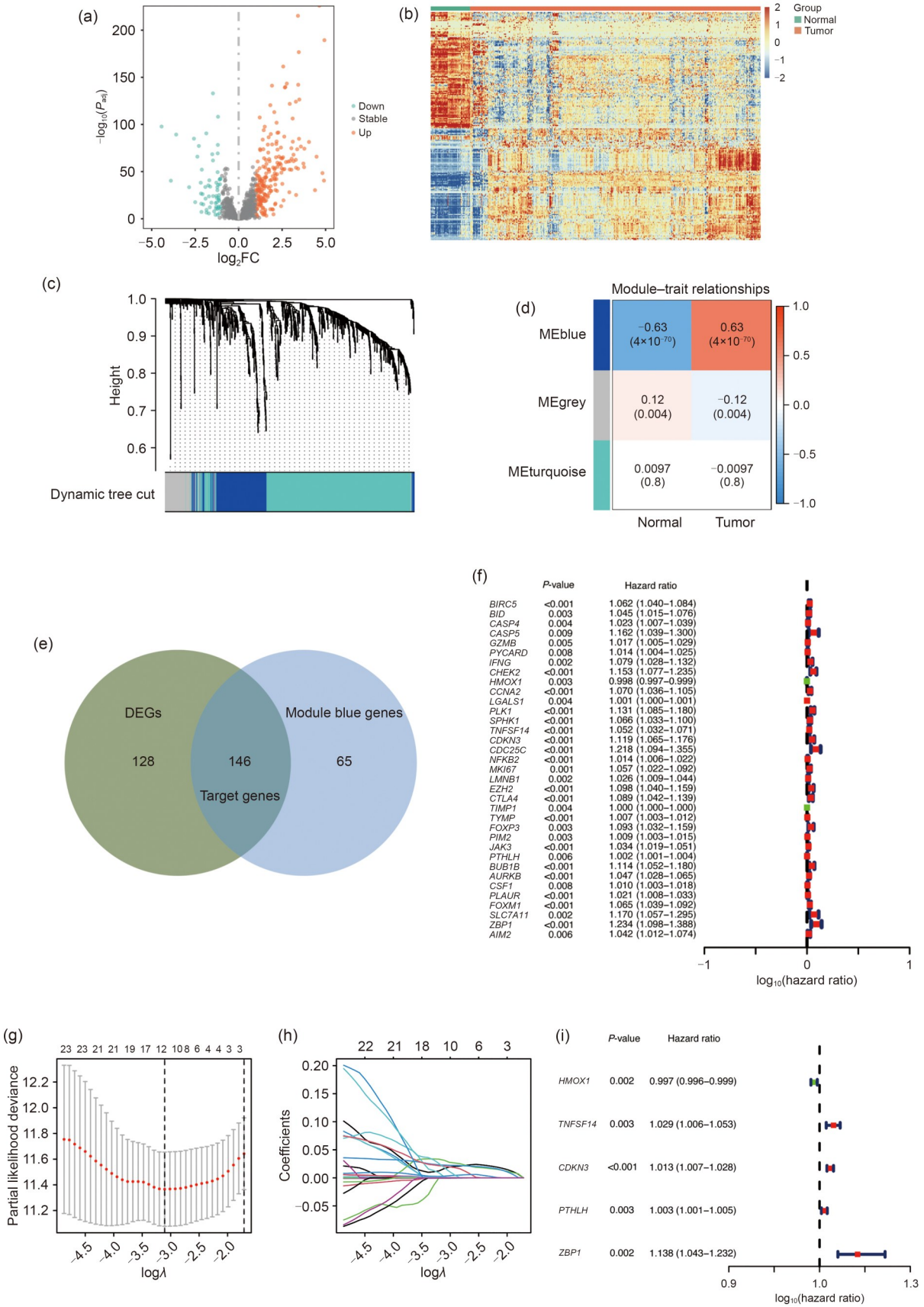
(a)
Down
Stable
Up
log2FC
(b)
Group
Normal
Tumor
(c)
Height
Dynamic tree cut
(d)
Module–trait relationships
MEblue
MEgrey
MEturquoise
−0.63 (4×10−70)
0.63 (4×10−70)
0.12 (0.004)
−0.12 (0.004)
0.0097 (0.8)
−0.0097 (0.8)
Normal
Tumor
(e)
DEGs
128
146
Target genes
Module blue genes
65
(f)
P-value
Hazard ratio
BIRC5 <0.001 1.062 (1.040–1.084)
BID 0.003 1.045 (1.015–1.076)
CASP4 0.004 1.023 (1.007–1.039)
CASP5 0.009 1.162 (1.039–1.300)
GZMB 0.005 1.017 (1.005–1.029)
PYCARD 0.008 1.014 (1.004–1.025)
IFNG 0.002 1.079 (1.028–1.132)
CHEK2 <0.001 1.153 (1.077–1.235)
HMOX1 0.003 0.998 (0.997–0.999)
CCNA2 <0.001 1.070 (1.036–1.105)
LGALS1 0.004 1.001 (1.000–1.001)
PLK1 <0.001 1.131 (1.085–1.180)
SPHK1 <0.001 1.066 (1.033–1.100)
TNFSF14 <0.001 1.052 (1.032–1.071)
CDKN3 <0.001 1.119 (1.065–1.176)
CDC25C <0.001 1.218 (1.094–1.355)
NFKB2 <0.001 1.014 (1.006–1.022)
MKI67 0.001 1.057 (1.022–1.092)
LMNB1 0.002 1.026 (1.009–1.044)
EZH2 <0.001 1.098 (1.040–1.159)
CTLA4 <0.001 1.089 (1.042–1.139)
TIMP1 0.004 1.000 (1.000–1.000)
TYMP <0.001 1.007 (1.003–1.012)
FOXP3 0.003 1.093 (1.032–1.159)
PIM2 0.003 1.009 (1.003–1.015)
JAK3 <0.001 1.034 (1.019–1.051)
PTHLH 0.006 1.002 (1.001–1.004)
BUB1B <0.001 1.114 (1.052–1.180)
AURKB <0.001 1.047 (1.028–1.065)
CSF1 0.008 1.010 (1.003–1.018)
PLAUR <0.001 1.021 (1.008–1.033)
FOXM1 <0.001 1.065 (1.039–1.092)
SLC7A11 0.002 1.170 (1.057–1.295)
ZBP1 <0.001 1.234 (1.098–1.388)
AIM2 0.006 1.042 (1.012–1.074)
log10(hazard ratio)
(g)
Partial likelihood deviance
logλ
(h)
Coefficients
logλ
(i)
P-value
Hazard ratio
HMOX1 0.002 0.997 (0.996–0.999)
TNFSF14 0.003 1.029 (1.006–1.053)
CDKN3 <0.001 1.013 (1.007–1.028)
PTHLH 0.003 1.003 (1.001–1.005)
ZBP1 0.002 1.138 (1.043–1.232)
log10(hazard ratio)

Fig. 1 Identification of candidate clear cell renal cell carcinoma (ccRCC)-specific pyroptosis, apoptosis, and necroptosis (PANoptosis)-related genes (PRGs) and construction of the prognostic PANoptosis-index (PANI). (a) Volcano plot of the differentially expressed genes (DEGs) in The Cancer Genome Atlas (TCGA), with the threshold set at $|\log_2 FC|>1$ (FC: fold change) and $P<0.05$. Upregulated DEGs are represented by orange dots, downregulated DEGs by green dots, and genes that are not significantly differentially expressed by gray dots. P_{adj}: adjusted P value. (b) Heatmap showing the expression profiles of the DEGs. (c) Tree of gene clusters. The dynamic tree-cutting approach was applied to discover modules by separating the tree diagram at significant branch points. This approach was based on an adjacency-based mismatch observed in the hierarchical gene clustering chart. Different colors have been assigned to each module, as indicated in the horizontal bar just below the tree diagram. (d) Associations between modules and traits in normal and malignant tissues. The table is structured so that each row represents a color module, while each column signifies a clinical characteristic. The correlation coefficient between each module and clinical features, along with the corresponding P value, is shown in the cells. (e) The Venn diagram is composed of ccRCC-specific DEGs and genes within the blue module associated with ccRCC. The 146 genes that overlap represent the candidate ccRCC-specific PRGs. (f) The forest plot illustrates the prognosis-associated PRGs as identified through univariate Cox proportional hazards regression analysis in ccRCC patients. (g) Penalties were calculated through one thousand rounds of cross-validation to determine the optimal parameter values. (h) The least absolute shrinkage and selection operator (LASSO)-Cox regression analysis was conducted, using the minimum criterion for parameter selection. λ is the penalty term, and the data above the graphs represent the number of non-zero coefficients (i.e., selected features/genes) in the model corresponding to each λ. (i) The forest plot shows the final set of prognostic PRGs established through multivariate Cox regression analysis in ccRCC patients.

3.2 Validation of expression profiles for prognostic PRGs

To evaluate the expression profiles of these prognostic PRGs, we first analyzed data from the TCGA database. The findings showed that these genes were significantly overexpressed in tumor tissues compared to normal tissues ($P<0.001$; Fig. 2a). We then measured the expression levels of the five PRGs in normal kidney and ccRCC cell lines using RT-qPCR (Figs. 2b–2f). Results indicated a pronounced increase in the messenger RNA (mRNA) levels of *ZBP1*, *TNFSF14*, *CDKN3*, *PTHLH*, and *HMOX1* in OS-RC-2 and 786-O cells compared to HK-2 cells. In A498 cells, *ZBP1*, *TNFSF14*, and *HMOX1* exhibited a significant rise in expression relative to HK-2 cells, whereas *PTHLH* and *CDKN3* did not show statistically significant increases.

Further examination of their expression profiles in scRNA-seq data revealed that gene set expression scores were markedly elevated in tumor cells compared to endothelial cells (Figs. 2g and 2h). Immunohistochemical analysis provided strong confirmation of *TNFSF14*, *PTHLH*, and *HMOX1* overexpression specific to ccRCC (Figs. S2a–S2c). Additionally, protein expression data reinforced the notable upregulation of HMOX1 in ccRCC and its strong association with both tumor grade and stage (Fig. S2d). Furthermore, *HMOX1*, identified as a favorable prognostic factor in ccRCC, showed higher expression levels in the low-PANI group (Fig. 2i). In contrast, the remaining genes, which are indicative of poorer prognosis in ccRCC patients, were significantly upregulated in the high-PANI group.

Additionally, the network of TFs and hub genes, including six TFs and two prognostic PRGs, was illustrated by a Sankey diagram (Fig. 2j). *ZBP1*, the PANoptosome trigger gene, was identified as regulated by three TFs associated with immune regulation, namely interferon regulatory factor 4 (IRF4), growth factor independence 1 (GFI1), and POU class 2 associating factor 1 (POU2AF1). Moreover, correlations between eRNAs and hub genes were predicted by Pearson correlation analysis to explore the underlying regulatory mechanisms in human malignancies. *CDKN3*, recognized as an adverse prognostic marker in ccRCC, showed the highest degree of connectivity and was controlled by five eRNAs (*AC015909.1*, *AF196972.1*, *AL669970.3*, *GAS1RR*, and *TENM3-AS1*) (Fig. 2k).

3.3 Validation of the prognostic signature and survival prediction

The prognostic signature developed from the training dataset was rigorously evaluated across multiple independent datasets, including the TCGA dataset, an internal test dataset, and an external validation set (E-MTAB-1980 cohort). KM analysis consistently showed that patients with high PANI scores had significantly poorer outcomes across all datasets (TCGA cohort: $P<0.001$, Fig. 3d; Training cohort: $P<0.001$, Fig. 3h; Testing cohort: $P=0.002$, Fig. 3l; E-MTAB-1980 cohort: $P=0.046$, Fig. 3p). Moreover, in the TCGA cohort, patients in the high-PANI group showed a markedly lower PFS rate compared to those in the low-PANI group, underscoring the predictive strength of the signature (Fig. 3e).

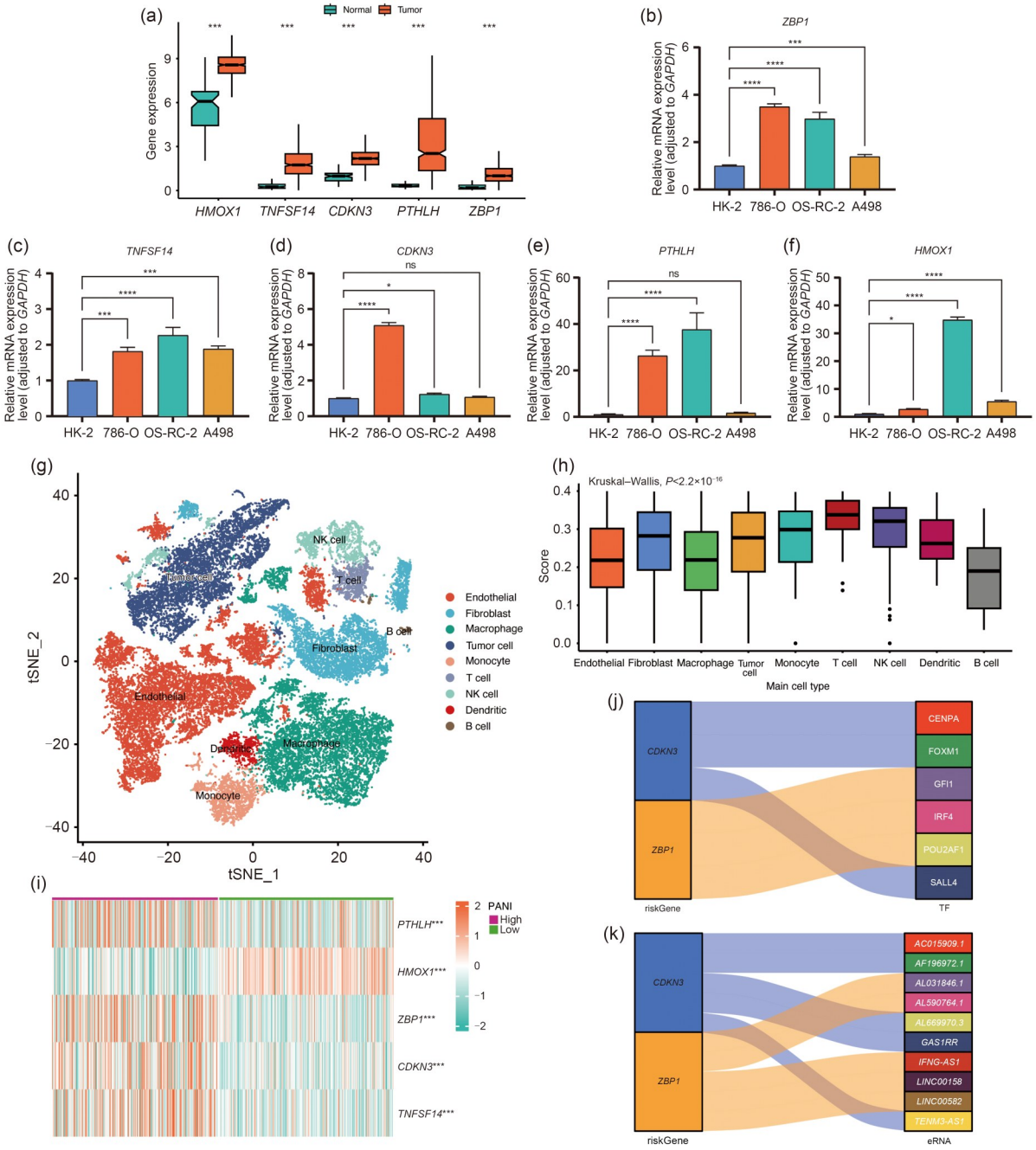

Fig. 2 Validation of prognostic pyroptosis, apoptosis, and necroptosis (PANoptosis)-related gene (PRG) expression profiles. (a) The expression profiles of the five PRGs in clear cell renal cell carcinoma (ccRCC) and normal kidney samples were compared using data from The Cancer Genome Atlas (TCGA) dataset. Wilcoxon rank-sum tests were used to assess the disparities in gene expression levels between tumor and normal samples. (b–f) Relative expression levels of the five PRGs in normal kidney cell lines and ccRCC cell lines were evaluated through reverse transcription-quantitative polymerase chain reaction (RT-qPCR). The data are expressed as mean±standard deviation (SD), *n*=3. *GAPDH*: glyceraldehyde 3-phosphate dehydrogenase. (g) A t-distributed stochastic neighbor embedding (t-SNE) visualization shows the single-cell RNA-sequencing (scRNA-seq) profiles obtained from clinical samples in the GSE156632 dataset. (h) The PANoptosis-index (PANI) signature score was computed across various cell types using data from the GSE156632 cohort. (i) A heatmap depicting the expression profiles of the five PRGs in the high- and low-PANI groups sourced from the TCGA dataset. (j) A Sankey diagram illustrating the potential regulatory relationships between PRGs and transcription factors (TFs). (k) A Sankey diagram illustrating the potential regulatory associations between PRGs and enhancer RNAs (eRNAs). * *P*< 0.05; * *P*<0.001; **** *P*<0.0001; ns, no statistical significance.**

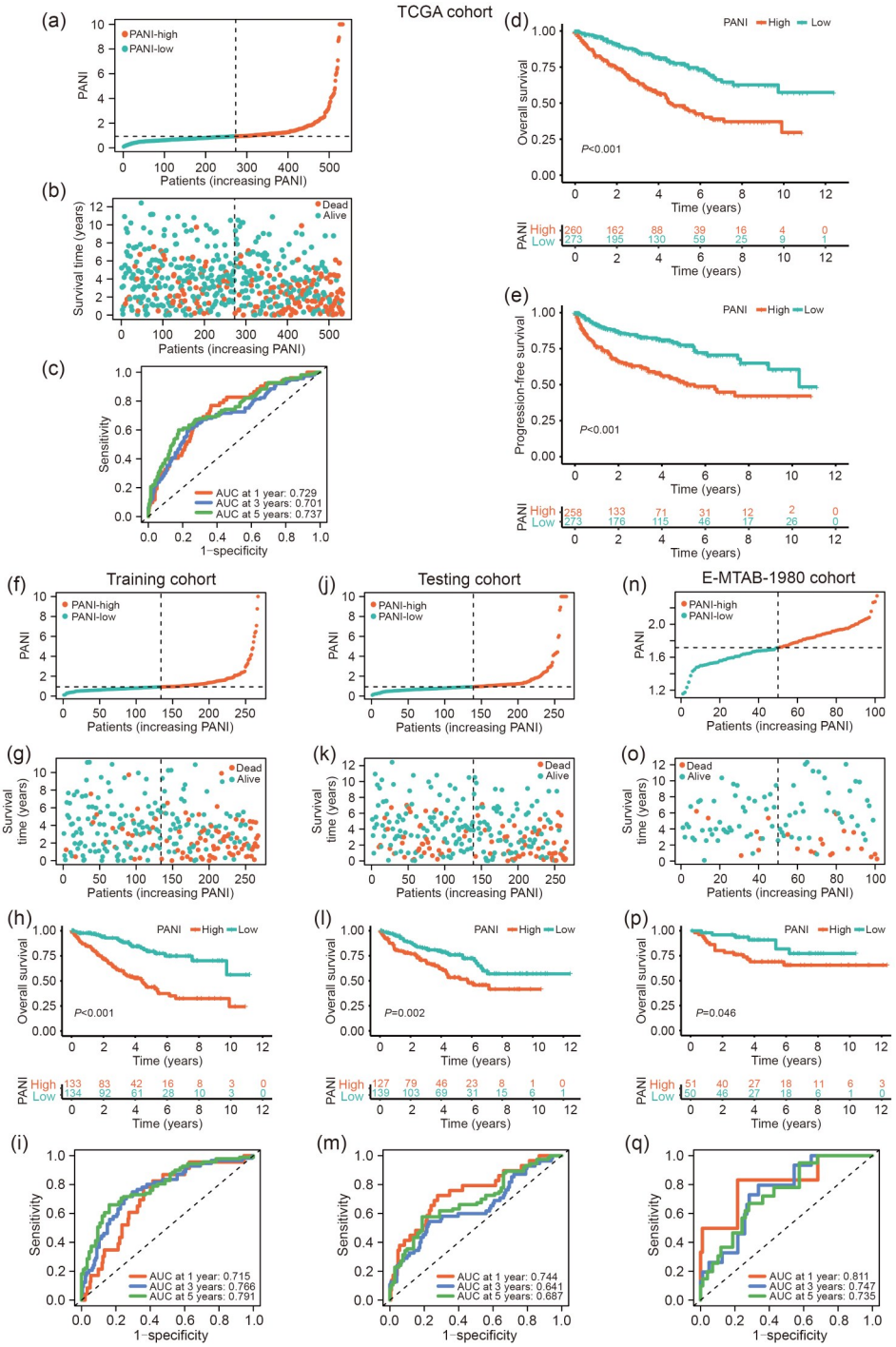

Fig. 3 Assessment and confirmation of the predictive performance of the pyroptosis, apoptosis, and necroptosis (PANoptosis)-related gene (PRG) signature in clear cell renal cell carcinoma (ccRCC). (a, f, j, n) The distribution of PANoptosis-index (PANI) in The Cancer Genome Atlas (TCGA) (a), training (f), testing (j), and E-MTAB-1980 external validation (n) cohorts. (b, g, k, o) Scatter plots illustrating the survival status and PANI scores of ccRCC patients in the TCGA (b), training (g), testing (k), and E-MTAB-1980 (o) cohorts. (d, h, l, p) Kaplan-Meier curves showing the overall survival (OS) situation per PANI score of the high- and low-PANI groups in the TCGA (d), training (h), testing (l), and E-MTAB-1980 (p) cohorts. (c, i, m, q) The receiver operating characteristic (ROC) curves showing the predictive performance of PANI with area under the curve (AUC) values for 1-, 3-, and 5-year OS in ccRCC patients from the TCGA (c), training (i), testing (m), and E-MTAB-1980 (q) cohorts. (e) Kaplan-Meier curves showing the progression-free survival situation per PANI score of the high- and low-PANI groups in the TCGA cohort.

To further substantiate the predictive accuracy, we conducted ROC curve analyses across the datasets. In the TCGA cohort, the AUC values for OS prediction at 1, 3, and 5 years were 0.729, 0.701, and 0.737, respectively (Fig. 3c). The corresponding values were 0.715, 0.766, and 0.791 in the training cohort, 0.744, 0.641, and 0.687 in the testing cohort, and 0.811, 0.747, and 0.735 in the E-MTAB-1980 cohort, respectively (Figs. 3i, 3m, and 3q). Collectively, these findings provide robust evidence that PANI is a reliable prognostic biomarker for ccRCC, with strong predictive power across diverse patient cohorts.

3.4 PANI-based clinical analysis and nomogram construction

The distribution of the PANI and its correlation with patient survival outcomes (Figs. 3a, 3b, 3f, 3g, 3j, 3k, 3n, and 3o) revealed a consistent trend across all four datasets. Higher PANI scores were positively associated with an increase in the proportion of high-risk patients and in the number of deaths. To confirm the clinical relevance of the PANI, we conducted both univariate and multivariate Cox regression analyses, incorporating clinical and pathological variables such as age, gender, pathological grade, clinical stage, and TNM (tumor, node, metastasis) stage. The results strongly indicated that PANI is an independent prognostic factor for ccRCC (P<0.001 and P=0.001; Figs. 4a and 4b).

Further analyses examined the distribution of PANI across various clinicopathological subgroups, including TNM stages and tumor grades. Significant differences in PANI levels were observed when comparing advanced grades and stages (e.g., Grade 4 versus other grades, Stage IV versus other stages, T4 stage versus other T stages), as well as in patients with distant metastasis (M1) and lymph node involvement (N1), who exhibited notably higher PANI scores than non-metastatic patients (M0 and N0) (P<0.05; Figs. 4c–4g). Finally, a stratified survival analysis was performed to evaluate the PANI's prognostic value within distinct clinicopathological subgroups.

To facilitate clinical application, we constructed a prognostic nomogram that integrates the PANI, tumor grade, and other clinical-pathological factors (Fig. 4i). Gender was excluded due to its negligible impact on outcomes (P=0.740 and P=0.553; Figs. 4a and 4b). ROC curve analysis showed the nomogram's reliable predictive performance, with AUCs of 0.814, 0.794, and 0.754 for 1-, 3-, and 5-year OS predictions, respectively (Fig. 4h). Calibration curves confirmed a strong concordance between the predicted and observed OS rates, suggesting high accuracy and clinical utility of the nomogram for patient prognosis in ccRCC (Fig. 4j).

3.5 Comparison of genomic alterations between the PANI groups

By integrating the mutation data of each patient, we conducted genomic mutation analysis for the PANI groups. In both high- and low-PANI groups, missense mutations were the predominant variant classification (Figs. S3a and S3g). Furthermore, among the variant types, single-nucleotide variants (SNVs) were the most prevalent, with C>T mutations being the primary SNV subtype (Figs. S3b, S3c, S3h, and S3i). Furthermore, to depict differences in the somatic mutation landscape between the two groups, we generated oncoplots that showed the contrasting mutational patterns observed in these two groups. In general, patients with a low PANI were found to have higher mutational frequencies (86.6% vs. 82.5%; Figs. 5a and 5b), with the median number of variants per patient in the low-PANI group being 46, compared to 43 in the high-PANI group (Figs. S3d and S3j). Furthermore, von Hippel-Lindau (*VHL*) and Polybromo1 (*PBRM1*) were the top two mutated genes in the two PANI groups, exhibiting distinct mutation frequencies (53% vs. 38% and 43% vs. 36%; Figs. S3f and S3l). Additionally, it was noteworthy that in the high-PANI group, gene mutations tended to co-occur more frequently than in the low-PANI group, where no co-occurrence events were evident (Figs. 5c and 5d). Notably, in the high-PANI group, the ccRCC-triggering gene *VHL* was found to co-occur with *PBRM1* and SET domain-containing 2 (*SETD2*), which are important co-drivers in ccRCC tumorigenesis (Walton et al., 2023), while being mutually exclusive with tumor protein p53 (*TP53*), a common tumor suppressor gene (Fig. 5c). Given that genomic alterations serve as crucial indicators of genomic instability, we conducted further investigations into the connection between PANI, TMB, and patient prognosis, and it became evident that patients with both high PANI and high TMB had the most unfavorable OS (P<0.001; Fig. S3n).

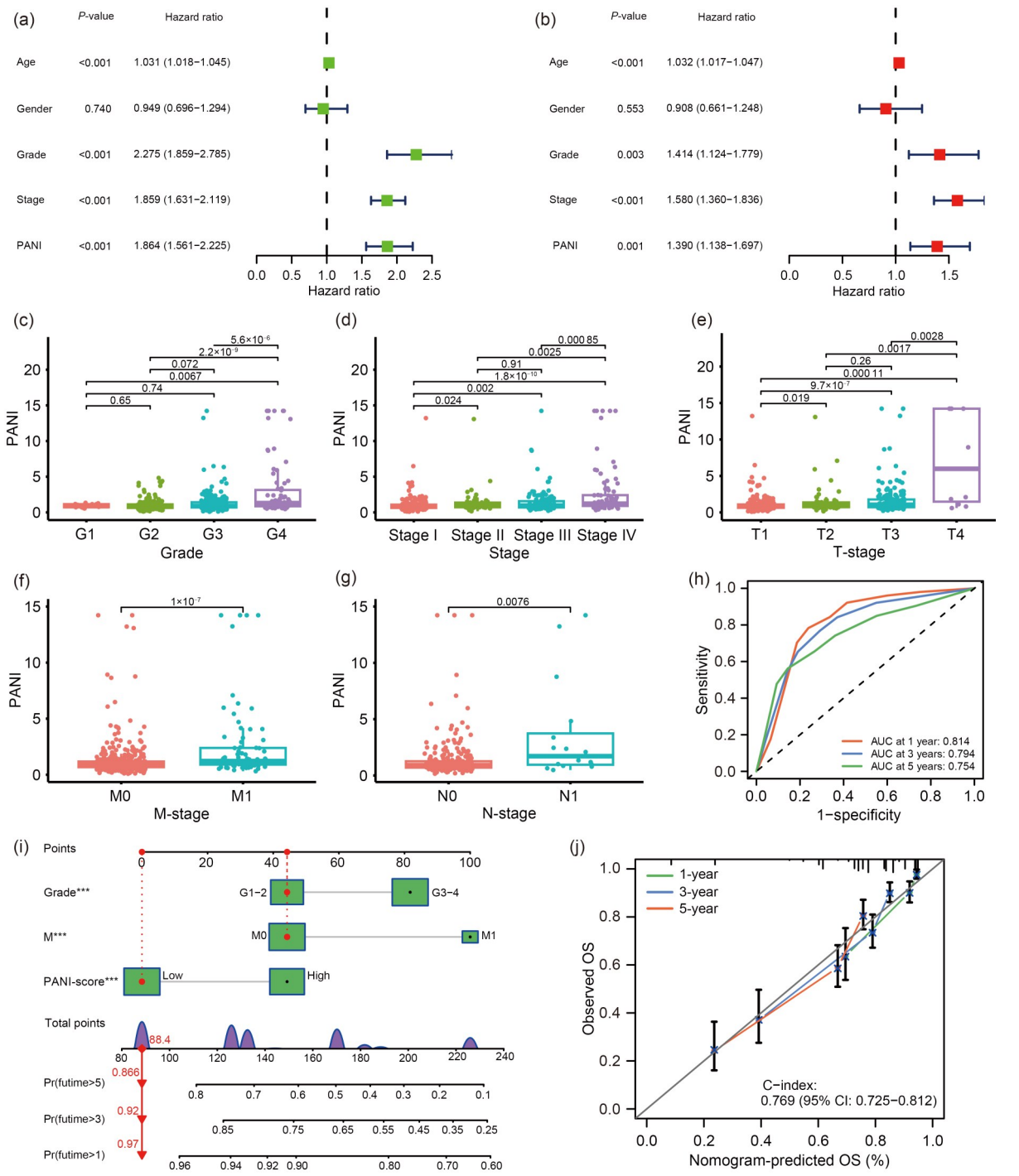

Fig. 4 Pyroptosis, apoptosis, and necroptosis (PANoptosis)-index (PANI)-based clinical analysis and construction of a nomogram that incorporates both clinical and pathological variables and the PANoptosis-related gene (PRG) signatures. (a) A univariate Cox regression examination of overall survival (OS)-related factors. (b) A multivariate Cox regression analysis of OS-related factors. (c–g) Wilcoxon rank-sum tests were used to assess the disparities in association with pathological grade (c), clinical stage (d), tumor (T) infiltration (e), distant metastasis (M) (f), and lymph node (N) involvement (g). (h) The nomogram-based receiver operating characteristic (ROC) curve analysis shows 1-, 3-, and 5-year OS and the corresponding area under the curve (AUC) values for clear cell renal cell carcinoma (ccRCC) patients from The Cancer Genome Atlas (TCGA) cohort. (i) The nomogram for prognostic prediction in ccRCC. Pr(futime>1), Pr(futime>3), and Pr(futime>5) represent the 1-, 3-, and 5-year survival probabilities, respectively. *** P<0.001. (j) The calibration curve used to verify the predictive performance of the signature. C-index: concordance index; CI: confidence Interval. The data are expressed as mean±standard deviation (SD), n=3.

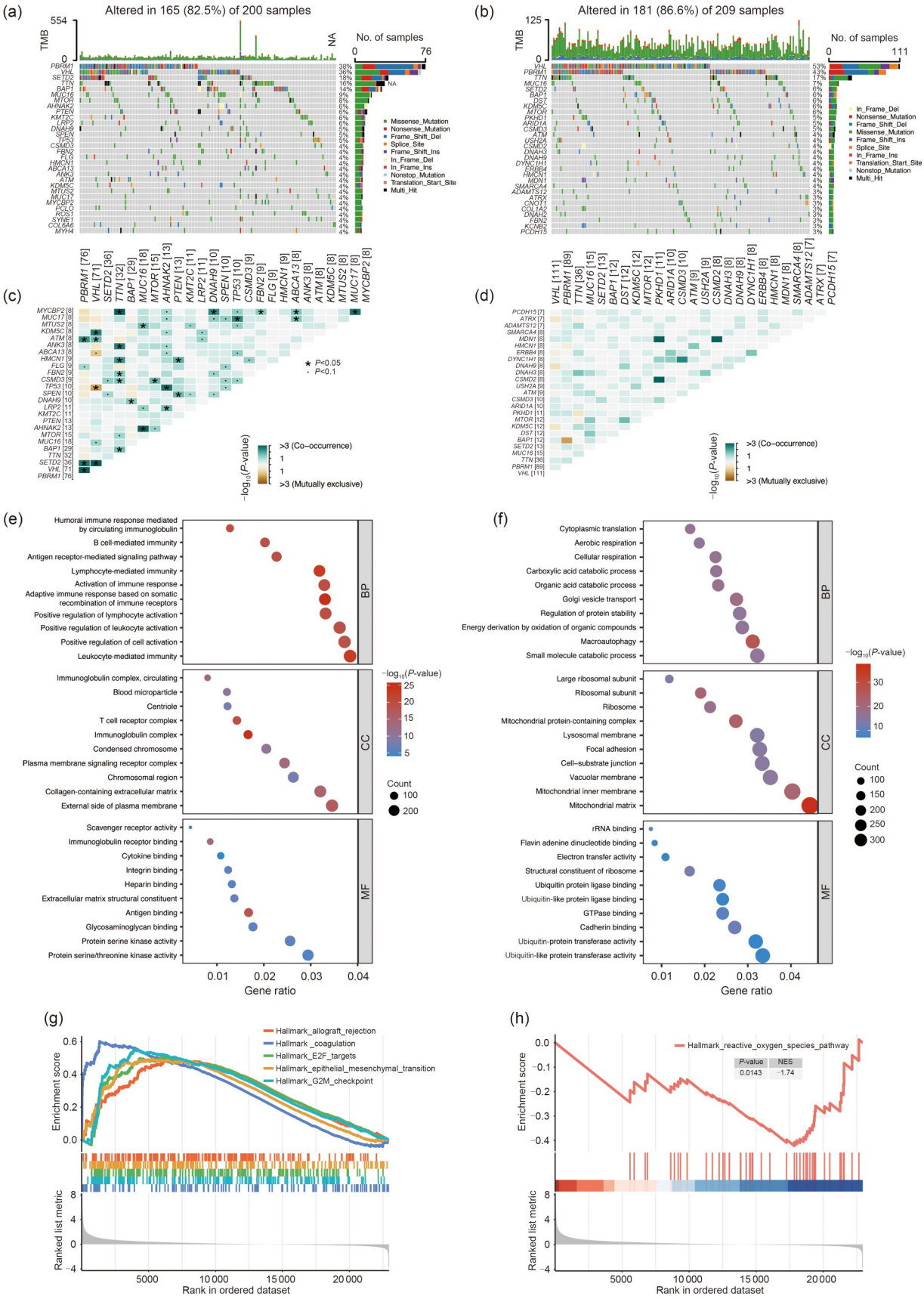
(a)
Altered in 165 (82.5%) of 200 samples
TMB
No. of samples
Missense_Mutation
Nonsense_Mutation
Frame_Shift_Del
Splice_Site
Frame_Shift_Ins
In_Frame_Del
In_Frame_Ins
Nonstop_Mutation
Translation_Start_Site
Multi_Hit
(b)
Altered in 181 (86.6%) of 209 samples
(c)
(d)
P<0.05
P<0.1
−log10(P-value)
>3 (Co−occurrence)
>3 (Mutually exclusive)
(e)
Humoral immune response mediated by circulating immunoglobulin
B cell-mediated immunity
Antigen receptor-mediated signaling pathway
Lymphocyte-mediated immunity
Activation of immune response
Adaptive immune response based on somatic recombination of immune receptors
Positive regulation of lymphocyte activation
Positive regulation of leukocyte activation
Positive regulation of cell activation
Leukocyte-mediated immunity
Immunoglobulin complex, circulating
Blood microparticle
Centriole
T cell receptor complex
Immunoglobulin complex
Condensed chromosome
Plasma membrane signaling receptor complex
Chromosomal region
Collagen-containing extracellular matrix
External side of plasma membrane
Scavenger receptor activity
Immunoglobulin receptor binding
Cytokine binding
Integrin binding
Heparin binding
Extracellular matrix structural constituent
Antigen binding
Glycosaminoglycan binding
Protein serine kinase activity
Protein serine/threonine kinase activity
BP
CC
MF
Count
Gene ratio
(f)
Cytoplasmic translation
Aerobic respiration
Cellular respiration
Carboxylic acid catabolic process
Organic acid catabolic process
Golgi vesicle transport
Regulation of protein stability
Energy derivation by oxidation of organic compounds
Macroautophagy
Small molecule catabolic process
Large ribosomal subunit
Ribosomal subunit
Ribosome
Mitochondrial protein-containing complex
Lysosomal membrane
Focal adhesion
Cell−substrate junction
Vacuolar membrane
Mitochondrial inner membrane
Mitochondrial matrix
rRNA binding
Flavin adenine dinucleotide binding
Electron transfer activity
Structural constituent of ribosome
Ubiquitin protein ligase binding
Ubiquitin-like protein ligase binding
GTPase binding
Cadherin binding
Ubiquitin-protein transferase activity
Ubiquitin-like protein transferase activity
(g)
Hallmark_allograft_rejection
Hallmark _coagulation
Hallmark_E2F_targets
Hallmark_epithelial_mesenchymal_transition
Hallmark_G2M_checkpoint
Enrichment score
Ranked list metric
Rank in ordered dataset
(h)
Hallmark_reactive_oxygen_species_pathway
P-value
NES
0.0143
-1.74

Fig. 5 Comparison of genomic alterations and functional enrichment analysis between the two pyroptosis, apoptosis, and necroptosis (PANoptosis)-index (PANI) groups. (a, b) The 30 most frequently mutated genes in the high- (a) and low-PANI (b) groups. (c, d) Heatmap illustrating the co-mutated states of the commonly mutated genes in the high- (c) and low-PANI (d) groups. (e, f) Functional enrichment analysis of upregulated genes in the high- (e) and low-PANI (f) groups based on gene ontology. (g, h) The gene set enrichment analysis (GSEA) based on hallmark gene sets, revealing the pathways enriched in the high- (g) and low-PANI (h) groups. TMB: tumor mutation burden; rRNA: ribosomal RNA; BP: biological process; MF: molecular function; CC: cellular component; NES: nuclear export signal.

3.6 Functional enrichment analysis of the PANI groups

To elucidate potential discrepancies in biological functions between different PANI groups, functional enrichment analyses based on the DEGs were introduced. Our analysis unveiled significant enrichments in several immune-related GO terms and pathways within the high-PANI group. These enrichments included terms related to the positive regulation of leukocyte activation, leukocyte-mediated immunity, lymphocyte activation, lymphocyte-mediated immunity, the T cell receptor complex, B cell-mediated immunity, immunoglobulin complex, and activation of the immune response, among others (Fig. 5e). Conversely, catabolism-related GO terms and pathways were notably enriched in the low-PANI group. These encompassed processes like small molecule catabolic process, organic acid catabolic process, and carboxylic acid catabolic process (Fig. 5f). Furthermore, the GSEA results highlighted a pronounced association of the high-PANI group with tumor progression. This association was reflected in hallmark pathways, for instance, E2F targets, epithelial mesenchymal transition, and the G2M checkpoint (Fig. 5g). In contrast, the low-PANI group was related to the reactive oxygen species pathway (Fig. 5h).

3.7 Comparison of TME between the PANI groups

The results from the GO functional enrichment analysis demonstrated a pronounced enrichment of immune pathways in the high-PANI group. To delve deeper into this observation, the ESTIMATE algorithm was used to evaluate the stromal scores, ESTIMATE scores, immune scores, and tumor purity of the ccRCC patients. The outcomes indicated a substantial difference, with the high-PANI group showing significantly higher immune scores (P<0.001) and ESTIMATE scores (P<0.01), compared with the low-PANI group. Furthermore, tumor purity was notably lower in the high-PANI group (P<0.01; Fig. 6b). These findings collectively suggested a substantial activation of the immune state in the high-PANI group. Notably, a high immune score indicated a poorer outcome in ccRCC (Fig. S4).

Next, we used a variety of algorithms to evaluate the tumor immune microenvironment comprehensively. We noticed a markedly elevated infiltration of immunocytes in the high-PANI group (Fig. 6a). This was reflected in a greater abundance of plasma cells, $CD8^+$ T cells, $CD4^+$ memory-activated T cells, follicular helper T cells, T regulatory cells (Tregs), and M1 macrophages (Fig. 6c). A barplot was used to provide the immune cell landscapes across all ccRCC patients (Fig. 6e). Furthermore, we compared the expression of various immunomodulators between the low- and high-PANI groups, including adhesion molecules, antigen presentation factors, co-stimulatory molecules, ligands, and other immunomodulatory markers. These molecules were upregulated in the high-PANI group (Fig. 6d). For further validation, ssGSEA was applied to evaluate the enrichment scores for immunocytes and the activity of immune-related pathways. These results provided additional confirmation of our previous discoveries, indicating that the high-PANI group not only exhibited increased immune cell infiltration but also heightened immune activation (Fig. 6f).

Furthermore, we created a butterfly plot to explore the relationships between PANI levels and the infiltration of immunocytes as well as immune functions. Apart from antigen-presenting cell (APC) co-stimulation and human leukocyte antigen (HLA) function, eleven other immune-related pathways exhibited significant correlations with PANI (Fig. 6g). Meanwhile, except for natural killer (NK) cells, macrophages, and follicular helper T cells, most immunocytes showed significant correlations with PANI (Fig. 6g). This outcome further validated the increased immunological activity within the high-PANI group. Additionally, we explored the correlations between prognostic PRGs and immunocyte infiltration, revealing that *ZBP1*, *CDKN3*, as well as *TNFSF14*, were positively related to the immune microenvironment (Fig. 6h).

3.8 Comparison of immunotherapy response between the PANI groups

Immune checkpoint inhibitors (ICIs) represent a promising category of cancer therapy drugs designed to enhance patients' immune function for combating tumor cell proliferation (Dutta et al., 2023). Considering the reported correlation between immune checkpoint gene (ICG) expression and the clinical effectiveness of ICIs, a comparative analysis of ICGs was performed in the high- and low-PANI groups. Our results unveiled substantial disparities in the expression of various ICGs between these PANI groups, highlighting distinct immunological profiles and effects of immunotherapy (Fig. 7a). Then, we looked into the relationships between two pivotal ICGs, programmed cell death 1 (*PDCD1*) and *CTLA4*, and PANI levels. This analysis revealed a significant association, showing that elevated PANI was closely linked to increased

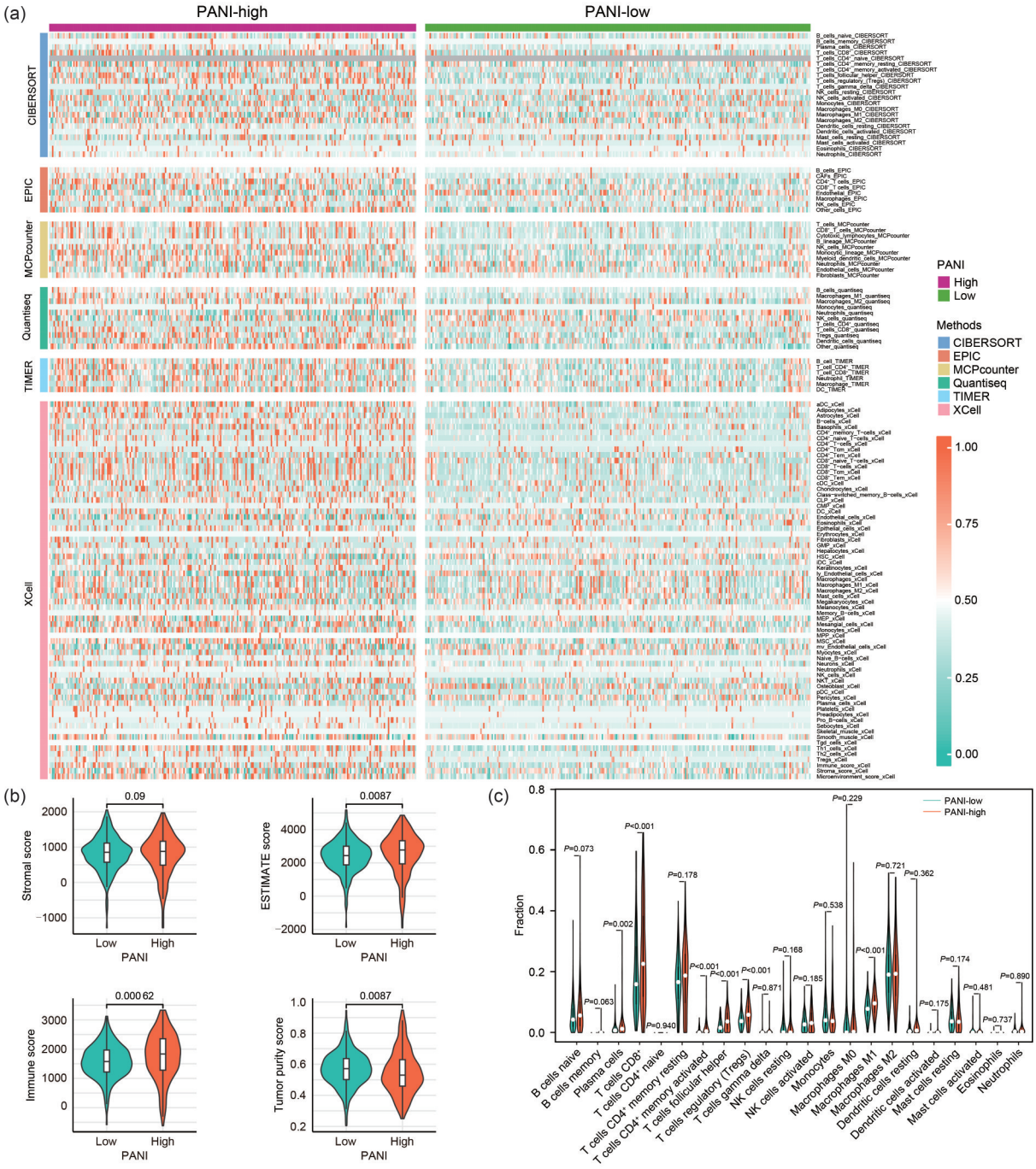

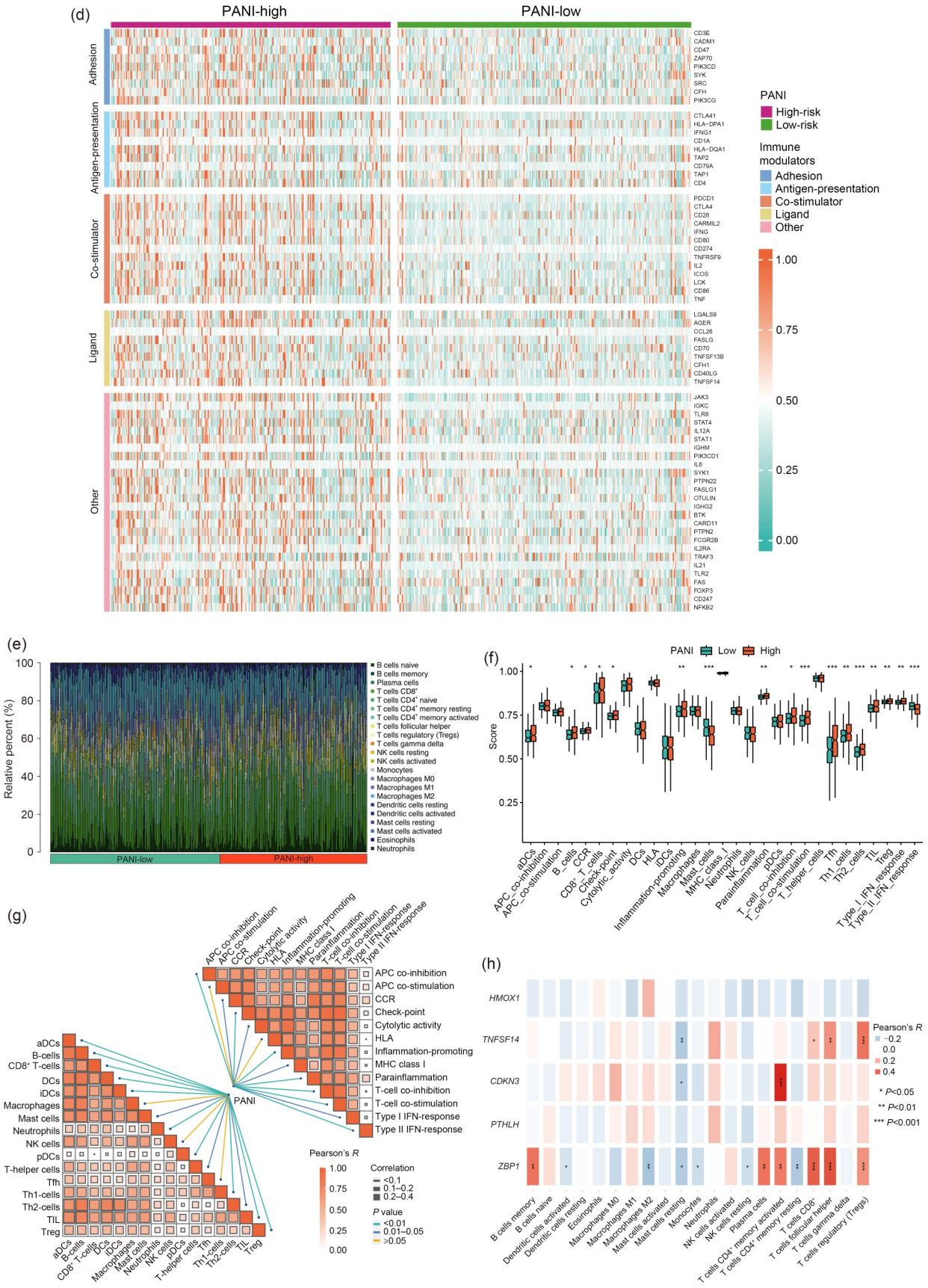
(d)
PANI-high
PANI-low
Adhesion
Antigen-presentation
Co-stimulator
Ligand
Other
CD3E
CADM1
CD47
ZAP70
PIK3CD
SYK
SRC
CFH
PIK3CG
CTLA41
HLA−DPA1
IFNG1
CD1A
HLA−DQA1
TAP2
CD79A
TAP1
CD4
PDCD1
CTLA4
CD28
CARMIL2
IFNG
CD80
CD274
TNFRSF9
IL2
ICOS
LCK
CD86
TNF
LGALS9
AGER
CCL26
FASLG
CD70
TNFSF13B
CFH1
CD40LG
TNFSF14
JAK3
IGKC
TLR8
STAT4
IL12A
STAT1
IGHM
PIK3CD1
IL6
SYK1
PTPN22
FASLG1
OTULIN
IGHG2
BTK
CARD11
PTPN2
FCGR2B
IL2RA
TRAF3
IL21
TLR2
FAS
FOXP3
CD247
NFKB2
PANI
High-risk
Low-risk
Immune modulators
Adhesion
Antigen-presentation
Co-stimulator
Ligand
Other
1.00
0.75
0.50
0.25
0.00
(e)
Relative percent (%)
100
80
60
40
20
0
PANI-low
PANI-high
B cells naive
B cells memory
Plasma cells
T cells CD8+
T cells CD4+ naive
T cells CD4+ memory resting
T cells CD4+ memory activated
T cells follicular helper
T cells regulatory (Tregs)
T cells gamma delta
NK cells resting
NK cells activated
Monocytes
Macrophages M0
Macrophages M1
Macrophages M2
Dendritic cells resting
Dendritic cells activated
Mast cells resting
Mast cells activated
Eosinophils
Neutrophils
(f)
PANI Low High
Score
1.00
0.75
0.50
0.25
aDCs
APC co-inhibition
APC co-stimulation
B cells
CCR
CD8+ T cells
Check-point
Cytolytic activity
DCs
HLA
iDCs
Inflammation-promoting
Macrophages
Mast cells
MHC class I
Neutrophils
NK cells
Parainflammation
pDCs
T cell co-inhibition
T cell co-stimulation
T helper cells
Tfh
Th1 cells
Th2 cells
TIL
Treg
Type I IFN response
Type II IFN response
(g)
APC co-inhibition
APC co-stimulation
CCR
Check-point
Cytolytic activity
HLA
Inflammation-promoting
MHC class I
Parainflammation
T-cell co-inhibition
T-cell co-stimulation
Type I IFN-response
Type II IFN-response
aDCs
B-cells
CD8+ T-cells
DCs
iDCs
Macrophages
Mast cells
Neutrophils
NK cells
pDCs
T-helper cells
Tfh
Th1-cells
Th2-cells
TIL
Treg
PANI
Pearson's R
1.00
0.75
0.50
0.25
0.00
Correlation
<0.1
0.1–0.2
0.2–0.4
P value
<0.01
0.01–0.05
≥0.05
(h)
HMOX1
TNFSF14
CDKN3
PTHLH
ZBP1
Pearson's R
−0.2
0.0
0.2
0.4
* P<0.05
** P<0.01
*** P<0.001
B cells memory
B cells naive
Dendritic cells activated
Dendritic cells resting
Eosinophils
Macrophages M0
Macrophages M1
Macrophages M2
Mast cells activated
Mast cells resting
Monocytes
Neutrophils
NK cells activated
NK cells resting
Plasma cells
T cells CD4+ memory activated
T cells CD4+ memory resting
T cells CD8+
T cells follicular helper
T cells gamma delta
T cells regulatory (Tregs)

Fig. 6 Comparative analysis of the tumor microenvironment between the two pyroptosis, apoptosis, and necroptosis (PANoptosis)-index (PANI) groups. (a) Heatmap illustrating the landscape of immune cell infiltration in the low- and high-PANI groups. (b) Comparison of stromal score, ESTIMATE score, immune score, and tumor purity in the low- and high-PANI groups. (c) Analysis of the fraction of infiltrating immune cells between the low- and high-PANI groups. (d) Heatmap showcasing the landscape of immune-related functions in the low- and high-PANI groups. (e) Boxplot showing the relative percentage of immune cells in each clear cell renal cell carcinoma (ccRCC) patient. (f) The single-sample gene set enrichment analysis (ssGSEA) of the disparities in immune infiltration levels and immune-related functions between the low- and high-PANI groups. (g) Butterfly plot illustrating the association between PANI and the fraction of immune cells and immune-related functions. (h) Heatmap depicting the association between the five PANoptosis-related genes (PRGs) and immune cells. *R*: correlation coefficient.

expression of these key immune checkpoints (Figs. 7b and 7c). This discovery further reinforced our conclusion that there are potential differences in the response to ICIs between the two PANI groups. Furthermore, the IPS difference analysis indicated that higher PANI patients, who were treated with either CTLA4 blocker monotherapy (P=0.045) or a combination therapy involving CTLA4 and PD-1/PD-L1/PD-L2 (P=0.011), might experience a more favorable outcome compared to individuals with lower PANI (Figs. 7d–7g). As we lacked access to data from ccRCC patients treated with immunotherapy, we obtained the IMvigor210 dataset, an external cohort comprising 348 patients who received anti-PD-1 therapy. This dataset was used to validate our prognostic PANI signature and offer indirect evidence for the prediction of immunotherapy efficacy in ccRCC patients. The analysis indicated that patients who achieved complete response (CR) or partial response (PR) exhibited elevated PANI levels (Fig. 7h). Conversely, a greater proportion of patients in the low-PANI group manifested either progressive disease (PD) or stable disease (SD) (Fig. 7i). These findings imply that individuals with heightened PANI levels had a higher possibility of benefiting from ICI therapy.

3.9 Antineoplastic drug sensitivity prediction

The sensitivity of the ccRCC population to antineoplastic drugs across various PANI groups was assessed by analyzing IC_{50} values. The high-PANI group had lower IC_{50} values, indicating increased sensitivity to several drugs, including the mammalian target of rapamycin (mTOR) inhibitor AZD2014, the pan-protein kinase B (pan-AKT) pathway inhibitor AZD5363, as well as poly(ADP-ribose) polymerase (PARP) inhibitors like talazoparib and olaparib (Figs. 7j–7n).

3.10 Identification of the carcinogenic effect of *ZBP1* on ccRCC

In our PANI, *ZBP1* exhibits a higher risk coefficient and is significantly overexpressed at the transcriptomic level in ccRCC patients (Fig. 2a), suggesting its potential carcinogenic effect. Consequently, we delved into the *ZBP1* gene. First, we confirmed the overexpression of *ZBP1* in ccRCC cell lines (Fig. 2b). Subsequently, we conducted RNA interference on 786-O and OS-RC-2 cells, followed by verification of the efficiency of *ZBP1* knockdown through RT-qPCR (Figs. 8a and 8b). Knockdown of *ZBP1* markedly suppressed the proliferation activity of ccRCC cells (Figs. 8c and 8d). Furthermore, Transwell and wound healing assays revealed a significant decrease in ccRCC cell migration post-*ZBP1* knockdown (Figs. 8e–8h), suggesting that *ZBP1* contributes to the progression of ccRCC.

4 Discussion

Neoplasms remain the main killer worldwide (Hu et al., 2016; Zhang XM et al., 2023). ccRCC is an intricate and heterogeneous malignancy, rendering the prediction of patient prognosis challenging. Advances in high-throughput sequencing and bioinformatics have furnished indispensable tools for investigating prognostic biomarkers, clinical stratification, and disease recurrence detection (Wang et al., 2009; Kyrochristos et al., 2019). Hence, it is of great importance to uncover clinically applicable prognostic biomarkers in ccRCC, with the aim of refining prognostic evaluations of disease progression, estimating OS, and customizing treatment strategies.

The expanding understanding of PCD mechanisms has revealed distinct molecular characteristics

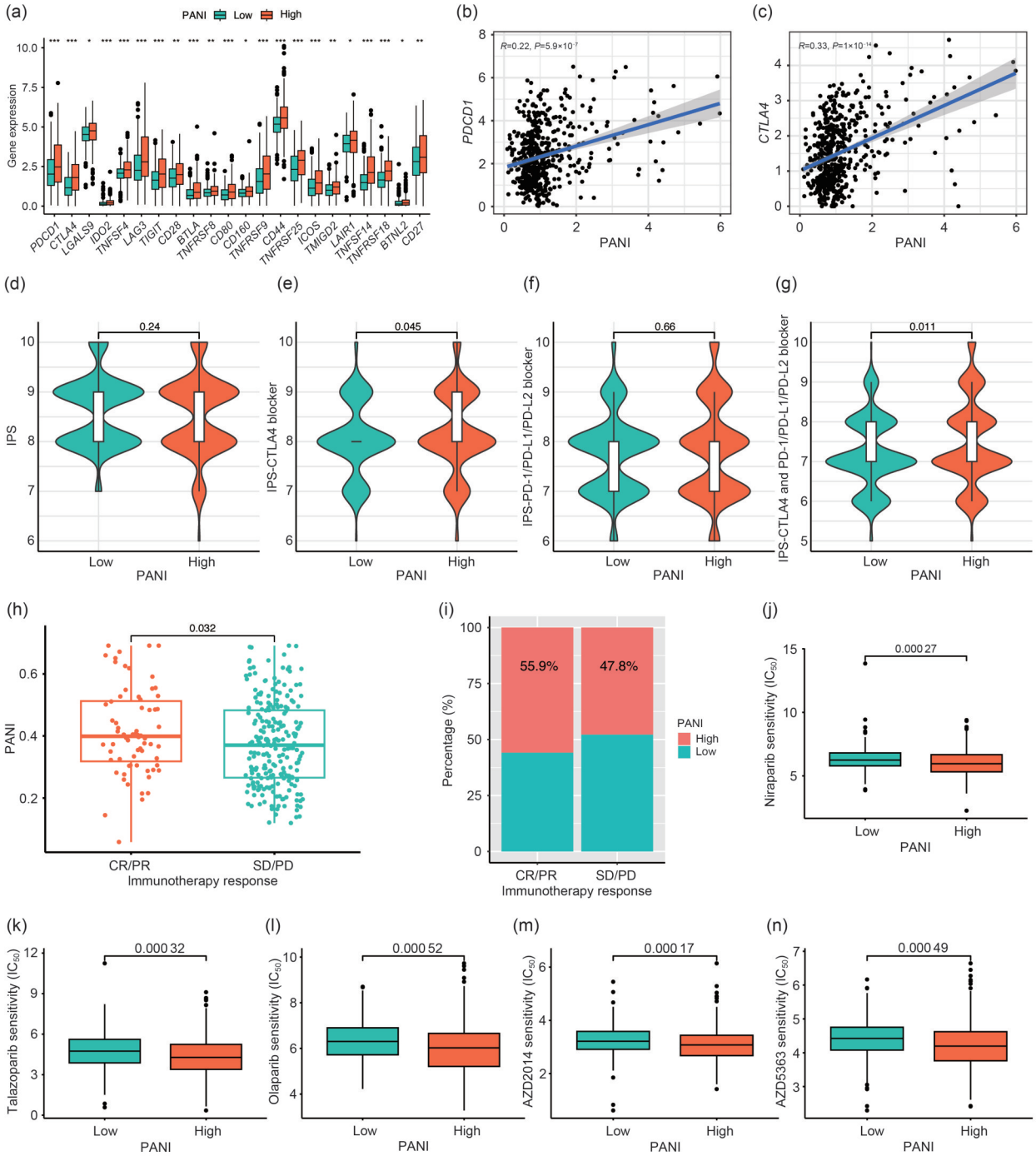

Fig. 7 Comparison of immunotherapy response and antineoplastic drug sensitivity between the two pyroptosis, apoptosis, and necroptosis (PANoptosis)-index (PANI) groups. (a) Boxplot illustrating the disparity in expression levels of immune checkpoint genes (ICGs) between the low- and high-PANI groups. * $P<0.05$; ** $P<0.01$; *** $P<0.001$. (b) Pearson correlation analysis revealing the association between PANI and programmed cell death 1 (*PDCD1*) expression. (c) Pearson correlation analysis revealing the association between PANI and cytotoxic T lymphocyte-associated antigen-4 (*CTLA4*) expression. (d–g) Violin plots depicting the disparities in response to immune checkpoint inhibitors (ICIs) between the low- and high-PANI groups. (h) Boxplot showing the distribution of PANI scores among clear cell renal cell carcinoma (ccRCC) patients with different immunotherapy responses. (i) Bar graph showing the percentage of responses to immunotherapy in the low- and high-PANI groups. (j–n) The half maximal inhibitory concentration (IC_{50}) values of antineoplastic drugs compared between the low- and high-PANI groups. PD-1: programmed cell death protein 1; PD-L1: programmed death-ligand 1; IPS: immunophenoscore; CR: complete response; PR: partial response; SD: stable disease; PD: progressive disease.

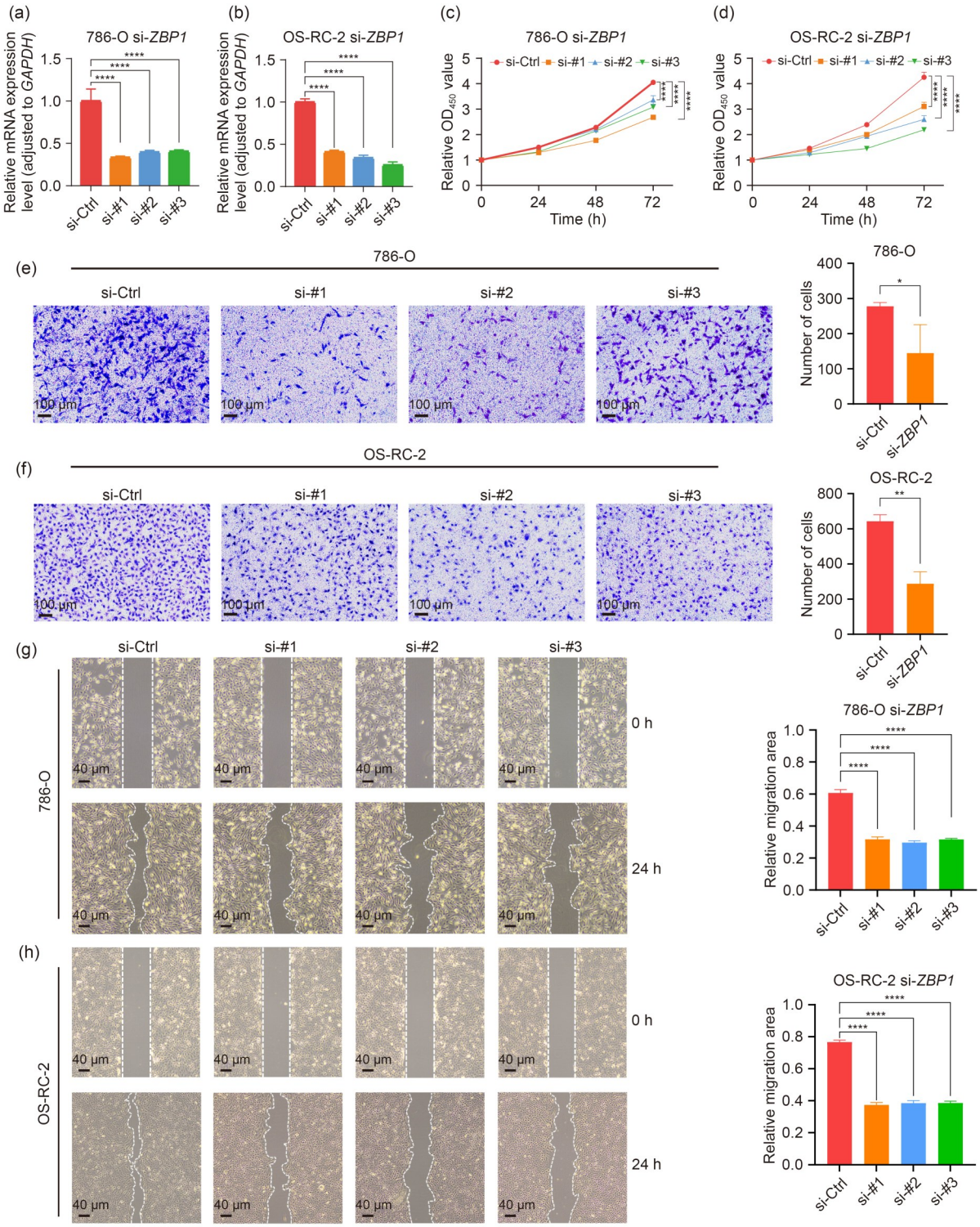

Fig. 8 Z-DNA-binding protein 1 (*ZBP1*) knockdown inhibits clear cell renal cell carcinoma (ccRCC) cell proliferation and migration. (a, b) The knockdown efficiencies of different small interfering RNA (siRNA)-*ZBP1* (si-*ZBP1*) constructs in 786-O and OS-RC-2 cells were evaluated using reverse transcription-quantitative polymerase chain reaction (RT-qPCR). (c, d) The effects of transfection with siRNA-#1 (si-#1), si-#2, si-#3, or negative control (si-Ctrl) on cell proliferation were evaluated using cell counting kit-8 (CCK-8) assays. (e–h) The effects of transfection with si-#1, si-#2, si-#3, or si-Ctrl on cell migration ability were evaluated using Transwell assays (e, f), and wound healing assays (g, h). The data are expressed as mean±standard deviation (SD), n=3. * P<0.05; ** P<0.01; *** P<0.001; **** P<0.0001. OD_{450}: optical density at 450 nm; mRNA: messenger RNA; GAPDH: glyceraldehyde 3-phosphate dehydrogenase.

inherent to various PCD pathways, leading to the concept of PANoptosis. PANoptosis is an intricately coordinated system characterized by complex interactions among multiple cell death pathways that regulate tumorigenesis (Ketelut-Carneiro and Fitzgerald, 2022). Unlike a single death pathway, PANoptosis functions through synergistic interactions within the same cell, either concurrently or sequentially (Karki et al., 2020; Chen et al., 2023). Moreover, various PCD pathways can complement one another, being triggered either simultaneously or sequentially in response to signals from the TME (Ketelut-Carneiro and Fitzgerald, 2022). For example, if apoptosis is inhibited in cancer cells undergoing immunotherapy, other PCD pathways like pyroptosis, necroptosis, or ferroptosis can be activated to eliminate cancer cells. The integration of these PCD pathways can significantly impact the immune microenvironment and tumor resistance. PANoptosis in cancer cells can trigger strong anti-cancer immune responses, and immunotherapy can work synergistically, even in cases of ICI resistance (Tang et al., 2020).

To predict the prognosis and immunotherapy effectiveness in ccRCC, we performed differential expression and WGCNA analysis on bulk transcriptomic data from renal cancer and normal kidney tissues, identifying 146 PRGs significantly associated with ccRCC. Using an integrated machine learning approach, we pinpointed five PRGs (*ZBP1*, *TNFSF14*, *CDKN3*, *PTHLH*, and *HMOX1*) that form the PANI for prognosis prediction. We validated the cancer-specific high expression of these PRGs through scRNA-seq data from clinical samples, immunohistochemistry from the HPA, and RT-qPCR in renal cancer cell lines. These results highlight the clinical potential of our PANI signature. Notably, *ZBP1*, an interferon-inducible protein and inflammasome sensor, has been recognized as a key instigator of PANoptosis, capable of activating the NLR family pyrin domain containing 3 (NLRP3) inflammasome and PANoptosome (Kuriakose et al., 2016; Lee et al., 2021). *ZBP1* plays a pivotal role in PANoptosis, and its deletion alone is sufficient to inhibit PANoptosis (Kuriakose et al., 2016). *TNFSF14*, a member of the tumor necrosis factor (TNF) family, is recognized for promoting T cell proliferation, supporting dendritic cell growth, and inducing apoptosis in cancer cells (Nallar et al., 2017). It has been shown to reverse immunosuppressive microenvironments and enhance anti-tumor immune responses (Ramachandran et al., 2023; Zhang N et al., 2023). *CDKN3* was verified to be able to promote cancer cell proliferation and is linked to tumor cell apoptosis (Yu et al., 2017; Li et al., 2022; Ma et al., 2023). While the role of *PTHLH* in PANoptosis remains underexplored, *HMOX1*, a key regulator of ferroptosis, plays a dual role in protection and cytotoxicity (Adedoyin et al., 2018; Chen et al., 2021; Tang et al., 2021). Normally, *HMOX1* exerts a protective role against PCD, but excessive *HMOX1* activity can induce cellular ferroptosis, referred to as atypical ferroptosis (Hassannia et al., 2018). To better understand the regulatory mechanisms behind the heightened expression of PRGs in ccRCC, we predicted the potential TFs and eRNAs involved in their regulation.

We successfully predicted PFS and OS outcomes for patients across the training, testing, and entire datasets using the PANI. External dataset validation further confirmed its reliability. Univariate and multivariate Cox regression analyses established PANI as an independent prognostic factor in ccRCC. Stratified analyses, incorporating various clinical variables, such as age, pathological stage, and grade, affirmed the broad clinical applicability of the model. Additionally, a diagnostic nomogram was developed and validated, incorporating PANI and key clinical features. The strong correlation between predicted and actual 1-, 3-, and 5-year OS in ccRCC patients underscores its potential as a clinically relevant prognostic tool.

PANoptosis is characterized by distinct features, such as plasma membrane rupture and the release of cellular contents, which trigger inflammatory responses through complex interactions among various cell death pathways (Ketelut-Carneiro and Fitzgerald, 2022). Our pathway enrichment analysis for the high-PANI group revealed significant enrichment in immune-related pathways. Additionally, a detailed analysis of the TME in the high-PANI group showed notable alterations, including increased immune scores, elevated ESTIMATE scores, and reduced tumor purity scores. Multiple algorithmic evaluations consistently highlighted increased immune cell infiltration and prolonged activation of immune functions, indicating a robust state of immune activation in the high-PANI group.

Furthermore, the high-PANI group also showed a significant upregulation of ICG, a higher IPS score for CTLA4 blockade, and increased responsiveness to CTLA4 and PD-1/PD-L1/PD-L2 blockade therapies,

along with a greater rate of CR or PR to immunotherapy. These findings strongly suggest that patients in the high-PANI group may experience enhanced effectiveness of ICIs. Overall, our PANI signature shows promise as a clinically valuable tool for predicting immune status and the responsiveness of ccRCC patients to immunotherapy. Additionally, the co-mutation of key driver genes of ccRCC, such as *VHL*, *PBRM1*, and *SETD2*, in the high-PANI group further emphasizes the association between PANI and tumor progression. GSEA revealed a significant enrichment of pathways related to tumor evolution in this group. This suggests that the accelerated tumor progression observed in the high-PANI group may contribute to its unfavorable prognosis, providing further insights into the molecular underpinnings of ccRCC progression.

We have successfully developed a prognostic index based on five PRGs, offering novel insights and potential biomarkers for predicting prognosis and immunotherapy effectiveness in ccRCC. However, there are some limitations to consider. Firstly, the study relied solely on data from the TCGA public database for model construction, highlighting the need for validation using larger and more diverse clinical datasets. Additionally, bulk RNA-seq data analysis may overlook intercellular differences and the complex interactions within the TME. To further validate the model, more open-access data on kidney cancer immunotherapy are needed. Lastly, further research is essential to explore and uncover the underlying mechanisms of PANoptosis in ccRCC and its potential therapeutic implications.

5 Conclusions

We have successfully developed PANI, a robust prognostic index that holds promise for enhancing prognosis prediction and guiding personalized treatment strategies in ccRCC. This signature, composed of five key PRGs (*ZBP1*, *TNFSF14*, *CDKN3*, *PTHLH*, and *HMOX1*), not only accurately predicts PFS and OS in ccRCC patients but also demonstrates its clinical applicability through validation in external datasets. Furthermore, PANI serves as an independent prognostic factor, even after stratification by various clinical factors. Our investigation revealed a strong correlation between PANI and immune-related pathways, indicating heightened immune activation marked by increased immunocyte infiltration and elevated immune functions within the high-PANI group. This group also exhibited increased ICG expression and a favorable response to ICIs, which bodes well for the potential efficacy of immunotherapy. Additionally, the co-mutation status of driver genes and pathway enrichment findings offer insights into the unfavorable prognosis observed in the high-PANI group. Moreover, we verified the carcinogenic effect of *ZBP1*, the most significant component of PANI, through in vitro experiments.

Data availability statement

The data presented in this study are publicly available in the NCBI Gene Expression Omnibus (GEO) repository (GSE156632), The Cancer Genome Atlas database (TCGA-KIRC, https://portal.gdc.cancer.gov), the Array Express database (E-MTAB-1980, https://www.ebi.ac.uk/arrayexpress), and a freely available, fully documented data package under the Creative Commons 3.0 license that can be downloaded from https://research-pub.gene.com/IMvigor210CoreBiologies. The datasets used or analyzed during the current study are available from the corresponding author upon reasonable request.

Acknowledgments

This work was supported by the Zhejiang Provincial Natural Science Foundation of China (No. LZ22H160008) and the Zhejiang Medical Science and Technology Project (Nos. 2022RC059 and 2023KY931), China. The authors extend their gratitude to all researchers who contributed to the public dataset employed in the study.

Author contributions

Yuyong WANG and Cheng ZHANG conceived and supervised the study; Yu DONG, Zitong YANG, Zhinan XIA, Jiahao LIAO, Zhiming CUI, and Shenhao XU designed and performed experiments; Yu DONG, Zitong YANG, Bing LIU, Liangliang REN, Tengda WANG, and Wei GUO analyzed the data; Shuwen WANG participated in manuscript revision; Yu DONG, Zitong YANG, and Zhinan XIA wrote the manuscript. All authors have read and approved the final manuscript, and therefore, have full access to all the data in the study and take responsibility for the integrity and security of the data.

Compliance with ethics guidelines

Yu DONG, Zitong YANG, Zhinan XIA, Jiahao LIAO, Zhiming CUI, Shenhao XU, Bing LIU, Liangliang REN, Tengda WANG, Wei GUO, Shuwen WANG, Yuyong WANG, and Cheng ZHANG declare that they have no conflicts of interest.

This article does not contain any studies with human or animal subjects performed by any of the authors.

References

Adedoyin O, Boddu R, Traylor A, et al., 2018. Heme oxygenase-1 mitigates ferroptosis in renal proximal tubule cells. *Amer J Physiol-Renal Physiol*, 314(5):F702-F714. https://doi.org/10.1152/ajprenal.00044.2017

Allemani C, Matsuda T, di Carlo V, et al., 2018. Global surveillance of trends in cancer survival 2000-14 (CONCORD-3): analysis of individual records for 37 513 025 patients diagnosed with one of 18 cancers from 322 population-based registries in 71 countries. *Lancet*, 391(10125):1023-1075. https://doi.org/10.1016/s0140-6736(17)33326-3

Aran D, Hu ZC, Butte AJ, 2017. xCell: digitally portraying the tissue cellular heterogeneity landscape. *Genome Biol*, 18:220. https://doi.org/10.1186/s13059-017-1349-1

Becht E, Giraldo NA, Lacroix L, et al., 2016. Estimating the population abundance of tissue-infiltrating immune and stromal cell populations using gene expression. *Genome Biol*, 17:218. https://doi.org/10.1186/s13059-016-1070-5

The Cancer Genome Atlas Research Network, 2013. Comprehensive molecular characterization of clear cell renal cell carcinoma. *Nature*, 499(7456):43-49. https://doi.org/10.1038/nature12222

Capitanio U, Montorsi F, 2016. Renal cancer. *Lancet*, 387(10021):894-906. https://doi.org/10.1016/s0140-6736(15)00046-x

Chen BB, Khodadoust MS, Liu CL, et al., 2018. Profiling tumor infiltrating immune cells with CIBERSORT. *Methods Mol Biol*, 1711:243-259. https://doi.org/10.1007/978-1-4939-7493-1_12

Chen W, Gullett JM, Tweedell RE, et al., 2023. Innate immune inflammatory cell death: PANoptosis and PANoptosomes in host defense and disease. *Eur J Immunol*, 53(11):2250235. https://doi.org/10.1002/eji.202250235

Chen X, Kang R, Kroemer G, et al., 2021. Organelle-specific regulation of ferroptosis. *Cell Death Differ*, 28(10):2843-2856. https://doi.org/10.1038/s41418-021-00859-z

Dall'Olio FG, Rizzo A, Mollica V, et al., 2021. Immortal time bias in the association between toxicity and response for immune checkpoint inhibitors: a meta-analysis. *Immunotherap*, 13(3):257-270. https://doi.org/10.2217/imt-2020-0179

Dutta S, Ganguly A, Chatterjee K, et al., 2023. Targets of immune escape mechanisms in cancer: basis for development and evolution of cancer immune checkpoint inhibitors. *Biology (Basel)*, 12(2):218. https://doi.org/10.3390/biology12020218

Ellis MJ, Gillette M, Carr SA, et al., 2013. Connecting genomic alterations to cancer biology with proteomics: the NCI clinical proteomic tumor analysis consortium. *Cancer Discov*, 3(10):1108-1112. https://doi.org/10.1158/2159-8290.Cd-13-0219

Friedman J, Hastie T, Tibshirani R, 2010. Regularization paths for generalized linear models via coordinate descent. *J Stat Softw*, 33(1):1-22. https://doi.org/10.18637/jss.v033.i01

Geeleher P, Cox N, Huang RS, 2014. pRRophetic: an R package for prediction of clinical chemotherapeutic response from tumor gene expression levels. *PLoS ONE*, 9(9):e107468. https://doi.org/10.1371/journal.pone.0107468

Gurung P, Anand PK, Subbarao Malireddi RK, et al., 2014. FADD and caspase-8 mediate priming and activation of the canonical and noncanonical Nlrp3 inflammasomes. *J Immunol*, 192(4):1835-1846. https://doi.org/10.4049/jimmunol.1302839

Guven DC, Sahin TK, Erul E, et al., 2022. The association between albumin levels and survival in patients treated with immune checkpoint inhibitors: a systematic review and meta-analysis. *Front Mol Biosci*, 9:1039121. https://doi.org/10.3389/fmolb.2022.1039121

Hänzelmann S, Castelo R, Guinney J, 2013. GSVA: gene set variation analysis for microarray and RNA-seq data. *BMC Bioinformatics*, 14:7. https://doi.org/10.1186/1471-2105-14-7

Hassannia B, Wiernicki B, Ingold I, et al., 2018. Nano-targeted induction of dual ferroptotic mechanisms eradicates high-risk neuroblastoma. *J Clin Invest*, 128(8):3341-3355. https://doi.org/10.1172/jci99032

Hu W, Yang Y, Fan CX, et al., 2016. Clinical and pathological significance of N-Myc downstream-regulated gene 2 (NDRG2) in diverse human cancers. *Apoptosis*, 21(6):675-682. https://doi.org/10.1007/s10495-016-1244-3

Jiang WY, Deng ZL, Dai XZ, et al., 2021. PANoptosis: a new insight into oral infectious diseases. *Front Immunol*, 12:789610. https://doi.org/10.3389/fimmu.2021.789610

Karki R, Sharma BR, Lee E, et al., 2020. Interferon regulatory factor 1 regulates PANoptosis to prevent colorectal cancer. *JCI Insight*, 5(12):e136720. https://doi.org/10.1172/jci.insight.136720

Karki R, Sundaram B, Sharma BR, et al., 2021a. ADAR1 restricts ZBP1-mediated immune response and PANoptosis to promote tumorigenesis. *Cell Rep*, 37(3):109858. https://doi.org/10.1016/j.celrep.2021.109858

Karki R, Sharma BR, Tuladhar S, et al., 2021b. Synergism of TNF-α and IFN-γ triggers inflammatory cell death, tissue damage, and mortality in SARS-CoV-2 infection and cytokine shock syndromes. *Cell*, 184(1):149-168.e17.

https://doi.org/10.1016/j.cell.2020.11.025

Ketelut-Carneiro N, Fitzgerald KA, 2022. Apoptosis, pyroptosis, and necroptosis—oh my! The many ways a cell can die. *J Mol Biol*, 434(4):167378. https://doi.org/10.1016/j.jmb.2021.167378

Kuriakose T, Man SM, Subbarao Malireddi RK, et al., 2016. ZBP1/DAI is an innate sensor of influenza virus triggering the NLRP3 inflammasome and programmed cell death pathways. *Sci Immunol*, 1(2):aag2045. https://doi.org/10.1126/sciimmunol.aag2045

Kyrochristos ID, Ziogas DE, Roukos DH, 2019. Dynamic genome and transcriptional network-based biomarkers and drugs: precision in breast cancer therapy. *Med Res Rev*, 39(3):1205-1227. https://doi.org/10.1002/med.21549

Lamkanfi M, Kanneganti TD, van Damme P, et al., 2008. Targeted peptidecentric proteomics reveals caspase-7 as a substrate of the caspase-1 inflammasomes. *Mol Cell Proteomics*, 7(12):2350-2363. https://doi.org/10.1074/mcp.M800132-MCP200

Langfelder P, Horvath S, 2008. WGCNA: an R package for weighted correlation network analysis. *BMC Bioinformatics*, 9:559. https://doi.org/10.1186/1471-2105-9-559

Lee S, Karki R, Wang YQ, et al., 2021. AIM2 forms a complex with pyrin and ZBP1 to drive PANoptosis and host defence. *Nature*, 597(7876):415-419. https://doi.org/10.1038/s41586-021-03875-8

Li AL, Cao CC, Gan Y, et al., 2022. ZNF677 suppresses renal cell carcinoma progression through N6-methyladenosine and transcriptional repression of CDKN3. *Clin Transl Med*, 12(6):e906. https://doi.org/10.1002/ctm2.906

Li TW, Fan JY, Wang BB, et al., 2017. TIMER: a web server for comprehensive analysis of tumor-infiltrating immune cells. *Cancer Res*, 77(21):e108-e110. https://doi.org/10.1158/0008-5472.Can-17-0307

Lin JF, Hu PS, Wang YY, et al., 2022. Phosphorylated NFS1 weakens oxaliplatin-based chemosensitivity of colorectal cancer by preventing PANoptosis. *Signal Transduct Target Ther*, 7:54. https://doi.org/10.1038/s41392-022-00889-0

Love MI, Huber W, Anders S, 2014. Moderated estimation of fold change and dispersion for RNA-seq data with DESeq2. *Genome Biol*, 15(12):550. https://doi.org/10.1186/s13059-014-0550-8

Lukens JR, Gurung P, Vogel P, et al., 2014. Dietary modulation of the microbiome affects autoinflammatory disease. *Nature*, 516(7530):246-269. https://doi.org/10.1038/nature13788

Ma J, Zhou WY, Yuan YF, et al., 2023. PSMD12 interacts with CDKN3 and facilitates pancreatic cancer progression. *Cancer Gene Ther*, 30(8):1072-1083. https://doi.org/10.1038/s41417-023-00609-y

Malireddi RK, Ippagunta S, Lamkanfi M, et al., 2010. Cutting edge: proteolytic inactivation of poly(ADP-ribose) polymerase 1 by the Nlrp3 and Nlrc4 inflammasomes. *J Immunol*, 185(6):3127-3130. https://doi.org/10.4049/jimmunol.1001512

Malireddi RK, Gurung P, Mavuluri J, et al., 2018. TAK1 restricts spontaneous NLRP3 activation and cell death to control myeloid proliferation. *J Exp Med*, 215(4):1023-1034. https://doi.org/10.1084/jem.20171922

Malireddi RK, Gurung P, Kesavardhana S, et al., 2020. Innate immune priming in the absence of TAK1 drives RIPK1 kinase activity-independent pyroptosis, apoptosis, necroptosis, and inflammatory disease. *J Exp Med*, 217(3):e20191644. https://doi.org/10.1084/jem.20191644

Mariathasan S, Turley SJ, Nickles D, et al., 2018. TGFβ attenuates tumour response to PD-L1 blockade by contributing to exclusion of T cells. *Nature*, 554(7693):544-548. https://doi.org/10.1038/nature25501

Mayakonda A, Lin DC, Assenov Y, et al., 2018. Maftools: efficient and comprehensive analysis of somatic variants in cancer. *Genome Res*, 28(11):1747-1756. https://doi.org/10.1101/gr.239244.118

Nallar SC, Xu DQ, Kalvakolanu DV, 2017. Bacteria and genetically modified bacteria as cancer therapeutics: current advances and challenges. *Cytokine*, 89:160-172. https://doi.org/10.1016/j.cyto.2016.01.002

Park HH, Kim HR, Park SY, et al., 2021. RIPK3 activation induces TRIM28 derepression in cancer cells and enhances the anti-tumor microenvironment. *Mol Cancer*, 20:107. https://doi.org/10.1186/s12943-021-01399-3

Plattner C, Finotello F, Rieder D, 2020. Deconvoluting tumor-infiltrating immune cells from RNA-seq data using quanTIseq. *Methods Enzymol*, 636:261-285. https://doi.org/10.1016/bs.mie.2019.05.056

Ramachandran M, Vaccaro A, van de Walle T, et al., 2023. Tailoring vascular phenotype through AAV therapy promotes anti-tumor immunity in glioma. *Cancer Cell*, 41(6):1134-1151.e10. https://doi.org/10.1016/j.ccell.2023.04.010

Rini BI, Battle D, Figlin RA, et al., 2019. The society for immunotherapy of cancer consensus statement on immunotherapy for the treatment of advanced renal cell carcinoma (RCC). *J Immunother Cancer*, 7:354. https://doi.org/10.1186/s40425-019-0813-8

Rizzo A, Mollica V, Tateo V, et al., 2023. Hypertransaminasemia in cancer patients receiving immunotherapy and immune-based combinations: the MOUSEION-05 study. *Cancer Immunol Immunother*, 72(6):1381-1394. https://doi.org/10.1007/s00262-023-03366-x

Rodriguez-Vida A, Hutson TE, Bellmunt J, et al., 2017. New treatment options for metastatic renal cell carcinoma. *ESMO Open*, 2(2):e000185. https://doi.org/10.1136/esmoopen-2017-000185

Santoni M, Buti S, Myint ZW, et al., 2024. Real-world outcome of patients with advanced renal cell carcinoma and intermediate- or poor-risk international metastatic renal cell carcinoma database consortium criteria treated by immune-oncology combinations: differential effectiveness by risk group? *Eur Urol Oncol*, 7(1):102-111. https://doi.org/10.1016/j.euo.2023.07.003

Sato Y, Yoshizato T, Shiraishi Y, et al., 2013. Integrated molecular analysis of clear-cell renal cell carcinoma. *Nat Genet*, 45(8):860-867. https://doi.org/10.1038/ng.2699

Stelzer G, Rosen N, Plaschkes I, et al., 2016. The geneCards suite: from gene data mining to disease genome sequence analyses. *Curr Protoc Bioinformatics*, 54:1.30.1-1.30.33. https://doi.org/10.1002/cpbi.5

Stuart T, Butler A, Hoffman P, et al., 2019. Comprehensive integration of single-cell data. *Cell*, 177(7):1888-1902.e21. https://doi.org/10.1016/j.cell.2019.05.031

Subramanian A, Tamayo P, Mootha VK, et al., 2005. Gene set enrichment analysis: a knowledge-based approach for interpreting genome-wide expression profiles. *Proc Natl Acad Sci USA*, 102(43):15545-15550. https://doi.org/10.1073/pnas.0506580102

Sun W, Li PC, Wang M, et al., 2023. Molecular characterization of PANoptosis-related genes with features of immune dysregulation in systemic lupus erythematosus. *Clin Immunol*, 253:109660. https://doi.org/10.1016/j.clim.2023.109660

Sung H, Ferlay J, Siegel RL, et al., 2021. Global cancer statistics 2020: GLOBOCAN estimates of incidence and mortality worldwide for 36 cancers in 185 countries. *CA A Cancer J Clinicians*, 71(3):209-249. https://doi.org/10.3322/caac.21660

Tang DL, Chen X, Kang R, et al., 2021. Ferroptosis: molecular mechanisms and health implications. *Cell Res*, 31(2): 107-125. https://doi.org/10.1038/s41422-020-00441-1

Tang R, Xu J, Zhang B, et al., 2020. Ferroptosis, necroptosis, and pyroptosis in anticancer immunity. *J Hematol Oncol*, 13:110. https://doi.org/10.1186/s13045-020-00946-7

Thomas PD, Ebert D, Muruganujan A, et al., 2022. PANTHER: making genome-scale phylogenetics accessible to all. *Protein Sci*, 31(1):8-22. https://doi.org/10.1002/pro.4218

Uhlén M, Fagerberg L, Hallström BM, et al., 2015. Tissue-based map of the human proteome. *Science*, 347(6220): 1260419. https://doi.org/10.1126/science.1260419

van Allen EM, Miao D, Schilling B, et al., 2015. Genomic correlates of response to CTLA-4 blockade in metastatic melanoma. *Science*, 350(6257):207-211. https://doi.org/10.1126/science.aad0095

Walton J, Lawson K, Prinos P, et al., 2023. PBRM1, SETD2 and BAP1–the trinity of 3p in clear cell renal cell carcinoma. *Nat Rev Urol*, 20(2):96-115. https://doi.org/10.1038/s41585-022-00659-1

Wang Z, Gerstein M, Snyder M, 2009. RNA-seq: a revolutionary tool for transcriptomics. *Nat Rev Genet*, 10(1): 57-63. https://doi.org/10.1038/nrg2484

Yoshihara K, Shahmoradgoli M, Martínez E, et al., 2013. Inferring tumour purity and stromal and immune cell admixture from expression data. *Nat Commun*, 4:2612. https://doi.org/10.1038/ncomms3612

Yu C, Cao HW, He XF, et al., 2017. Cyclin-dependent kinase inhibitor 3 (CDKN3) plays a critical role in prostate cancer via regulating cell cycle and DNA replication signaling. *Biomed Pharmacother*, 96:1109-1118. https://doi.org/10.1016/j.biopha.2017.11.112

Zhang M, Zhai W, Miao JJ, et al., 2022. Single cell analysis reveals intra-tumour heterogeneity, microenvironment and potential diagnosis markers for clear cell renal cell carcinoma. *Clin Transl Med*, 12(5):e713. https://doi.org/10.1002/ctm2.713

Zhang N, Liu XH, Qin JL, et al., 2023. LIGHT/TNFSF14 promotes CAR-T cell trafficking and cytotoxicity through reversing immunosuppressive tumor microenvironment. *Mol Ther*, 31(9):2575-2590. https://doi.org/10.1016/j.ymthe.2023.06.015

Zhang XM, Yu SS, Li XB, et al., 2023. Research progress on the interaction between oxidative stress and platelets: another avenue for cancer? *Pharmacol Res*, 191: 106777. https://doi.org/10.1016/j.phrs.2023.106777

Zhao PF, Wang M, Chen M, et al., 2020. Programming cell pyroptosis with biomimetic nanoparticles for solid tumor immunotherapy. *Biomaterials*, 254:120142. https://doi.org/10.1016/j.biomaterials.2020.120142

Zheng M, Karki R, Vogel P, et al., 2020. Caspase-6 is a key regulator of innate immunity, inflammasome activation, and host defense. *Cell*, 181(3):674-687.e13. https://doi.org/10.1016/j.cell.2020.03.040

Supplementary information

Tables S1 and S2; Figs. S1–S4